

Scaling Law of Neural Koopman Operators

Abulikemu Abuduweili*, Yuyang Pang*, Feihan Li, and Changliu Liu

Abstract—Data-driven neural Koopman operator theory has emerged as a powerful tool for linearizing and controlling nonlinear robotic systems. However, the performance of these data-driven models fundamentally depends on the trade-off between sample size and model dimensions, a relationship for which the scaling laws have remained unclear. This paper establishes a rigorous framework to address this challenge by deriving and empirically validating scaling laws that connect sample size, latent space dimension, and downstream control quality. We derive a theoretical upper bound on the Koopman approximation error, explicitly decomposing it into sampling error and projection error. We show that these terms decay at specific rates relative to dataset size and latent dimension, providing a rigorous basis for the scaling law. Based on the theoretical results, we introduce two lightweight regularizers for the neural Koopman operator: a covariance loss to help stabilize the learned latent features and an inverse control loss to ensure the model aligns with physical actuation. The results from systematic experiments across six robotic environments confirm that model fitting error follows the derived scaling laws, and the regularizers improve dynamic model fitting fidelity, with enhanced closed-loop control performance. Together, our results provide a simple recipe for allocating effort between data collection and model capacity when learning Koopman dynamics for control.

Index Terms—Nonlinear Control, Dynamics Model, Koopman Operator Theory, Scaling Law

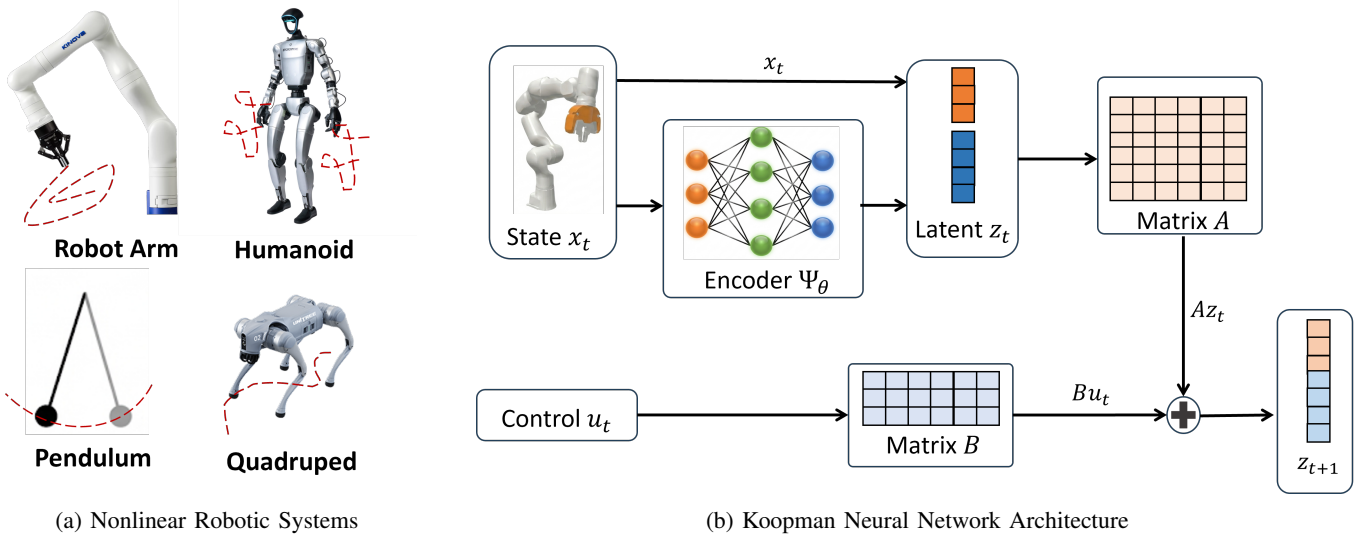
I. INTRODUCTION

Controlling nonlinear dynamical systems remains a central challenge in robotics and control theory [1]. Two dominant paradigms have emerged to address this challenge. Model-free control, including model-free Reinforcement Learning (RL), delivers remarkable task-level performance in complex domains like legged locomotion [2], but is hampered by its high sample complexity and highly task-specific controllers that require retraining for new tasks or varying dynamics [3], [4]. In contrast, model-based approaches [5] decouple the dynamics modeling from control, allowing a general-purpose dynamics model to be reused across various downstream tasks. Within this paradigm, direct methods like nonlinear model predictive control (MPC), tackle the full dynamics but require solving computationally expensive, nonconvex optimization at each time step [6], [7]. Local linearization methods, such as iterative LQR, are more efficient but are only reliable near a nominal trajectory and can degrade unpredictably when the system deviates [8], [9]. Addressing these deviations often requires sophisticated adaptation mechanisms to maintain model

fidelity under uncertainty [10], [11]. This trade-off motivates our focus: global linearization techniques, which represent complex nonlinear dynamics as globally valid linear systems in a higher-dimensional ‘lifted’ latent space. By paying a one-time offline modeling cost, these methods enable the use of efficient and powerful linear control techniques for real-time execution.

Originating in the 1930s [12], Koopman operator theory analyzes the evolution of observable (embedding) functions in the latent state, rather than tracking states in an original nonlinear space. It establishes that an infinite-dimensional linear operator governs this latent evolution, allowing full nonlinear systems to be analyzed with linear theory in a lifted function space [13]. This framework is widely applied across fields like fluid dynamics [14], power systems, and molecular dynamics. Practical applications rely on data-driven methods that seek a finite-dimensional approximation of the Koopman operator via Extended Dynamic Mode Decomposition (EDMD) [15]. EDMD requires a user-specified dictionary of basis functions (e.g., polynomials, radial basis functions) to define the latent space of observables, then computes a finite-dimensional linear operator (matrix) via least-squares regression. Consequently, EDMD’s success hinges entirely on dictionary selection, and its scalability is limited by the curse of dimensionality, as the number of basis functions often grows exponentially with the system’s state dimension [16]. To overcome this limitation, recent research uses deep neural networks to *learn* the observable functions directly from data. In this paradigm, often termed **Neural Koopman**, a neural network embedding function maps the original state into a latent space of observables. The entire model is trained end-to-end to simultaneously discover a set of basis functions (the embedding) and the linear operator governing the latent dynamics [17], [18]. This synergy between Koopman theory and deep learning has enabled significant progress in robotics, with applications ranging from motion planning [19] to real-time, low-level control [20], [21]. Parallel theoretical efforts seek to rigorize these data-driven approximations. Recent works derive quantitative finite-data error bounds linking the error to the dictionary richness [22], establish spectral convergence rates to address spurious eigenvalues [23], and propose spectral regularizers enforcing Lyapunov stability [24]. However, these analyses typically rely on fixed dictionaries or asymptotic arguments, leaving the finite-sample behavior of *neural* approximations largely uncharacterized. On the other hand, integrating learned Koopman models with linear MPC has achieved high-fidelity tracking on challenging quadrupedal and humanoid systems [25], [26]. Despite these empirical successes, a formal connection between Koopman operator

Authors are with the Robotics Institute, Carnegie Mellon University, Pittsburgh, PA 15213, USA. (abulikea, yuyangp, feihanl, cliu6)@andrew.cmu.edu. *Equal contributions.



(a) Nonlinear Robotic Systems (b) Koopman Neural Network Architecture
 Fig. 1: Overview. (a) Mechanical systems (e.g., robot arm, quadruped) exhibiting complex nonlinear dynamics in physical state space. (b) Our proposed Koopman architecture uses an encoder network Ψ_θ to map the physical state x_t into a latent space z_t , governed by linear dynamics: $z_{t+1} = \mathbf{A}z_t + \mathbf{B}u_t$.

theory and the practical performance of finite-sample, finite-capacity models remains lacking. This paper bridges exactly this gap.

However, the performance of these data-driven methods fundamentally depends on the interplay between training sample size and the model’s embedding dimension. This observation is analogous to the study of **neural scaling laws** in deep learning, where model performance has been shown to scale predictably as a power-law of data, model size, and compute [27], [28]. In robotics, recent large-scale studies have empirically validated these scaling properties for imitation learning and offline reinforcement learning [29]–[31]. However, a systematic theoretical study for data-driven Koopman operators remains absent. Consequently, practitioners face critical questions: to improve an underperforming model, should one invest in more data or greater capacity? How much does error decrease with each resource, and is the expected gain worth the cost? To answer these questions and guide design, this paper derives and empirically validates scaling laws for neural Koopman operators. Our key contributions are: **1) A theoretical framework** establishing scaling laws for Koopman approximation error, decomposed into data- and model-dependent terms with explicit decay rates and underlying assumptions; **2) Two lightweight regularizers**, motivated by our theory, that significantly enhance model learning and closed-loop control; and **3) Systematic experiments** across six robotic tasks validating the theoretical scaling laws and demonstrating the regularizers’ effectiveness in model predictive control (MPC). Scripts are available at <https://github.com/intelligent-control-lab/Koopman-Scaling>.

II. PRELIMINARY: KOOPMAN OPERATOR THEORY

We briefly overview the Koopman operator framework. Consider a discrete-time, nonlinear autonomous system (e.g., the robotic platforms in fig. 1a) governed by: $s^+ = f(s)$ for $s \in \mathcal{S}$, where $s \in \mathcal{S}$ is the state and s^+ is the transitioned state. Koopman theory analyzes this system by embedding the state

into a latent space with linear dynamics via a vector-valued (observable) **embedding function**, $\Phi^* : \mathcal{S} \rightarrow \mathcal{O}$. The infinite-dimensional Koopman operator \mathcal{K} propagates the latent state **linearly** forward in time:

$$(\mathcal{K}\Phi^*)(s) = \Phi^*(f(s)). \quad (1)$$

For a controlled system $x^+ = f(x, u)$ with state $x \in \mathcal{X} \subset \mathbb{R}^{n_x}$ and control input $u \in \mathcal{U} \subset \mathbb{R}^{n_u}$, We linearly approximate the state-dependent evolution by lifting state x to a finite-dimensional subspace \mathbb{R}^n via an embedding $\Phi(x)$ and treating u as an exogenous input. We define a lifted state-control vector φ that concatenates the observables with the inputs:

$$\varphi(x, u) := \begin{bmatrix} \Phi(x) \\ u \end{bmatrix} \in \mathbb{R}^{n+n_u}, \quad \text{with } \Phi : \mathbb{R}^{n_x} \rightarrow \mathbb{R}^n. \quad (2)$$

Approximating the Koopman operator \mathcal{K} with a matrix \mathbf{K} yields the lifted linear dynamics:

$$\begin{bmatrix} \Phi(x^+) \\ u^+ \end{bmatrix} \approx \mathbf{K} \begin{bmatrix} \Phi(x) \\ u \end{bmatrix} = \begin{bmatrix} \mathbf{A} & \mathbf{B} \\ \mathbf{C} & \mathbf{D} \end{bmatrix} \begin{bmatrix} \Phi(x) \\ u \end{bmatrix} \quad (3)$$

For control, we focus on the evolution of state-dependent latent variables $\Phi(x)$, treating the control sequence $\{u\}$ as an independent external input. This simplifies the matrix equation’s top row to the widely used linear dynamics model:

$$\Phi(x^+) = \mathbf{A}\Phi(x) + \mathbf{B}u \quad (4)$$

where $\mathbf{A} \in \mathbb{R}^{n \times n}$ governs autonomous observable evolution and $\mathbf{B} \in \mathbb{R}^{n \times n_u}$ captures actuation effects.

To avoid degenerate trivial solutions (e.g., $\mathbf{A} = \mathbf{B} = 0$ with $\Phi \equiv 0$) and preserve the physical interpretation of the state, we augment the physical state into the embedding, as shown in fig. 1(b):

$$z := \Phi_\theta(x) = \begin{bmatrix} x \\ \Psi_\theta(x) \end{bmatrix}, \quad \Psi_\theta : \mathbb{R}^{n_x} \rightarrow \mathbb{R}^{n-n_x} \quad (5)$$

where the full embedding Φ_θ concatenates x with residual nonlinear features learned by the neural encoder Ψ_θ . Since the latent vector strictly contains the physical state, x is perfectly

recovered via a fixed linear projection \mathbf{P} :

$$x = \mathbf{P}z = \mathbf{P}\Phi_\theta(x), \quad \mathbf{P} = [\mathbf{I}_{n_x}, \mathbf{0}_{n_x \times (n-n_x)}] \in \mathbb{R}^{n_x \times n} \quad (6)$$

This construction enables state-constrained formulations to be expressed directly in the latent space while retaining linear system evolution. Both the embedding function Φ_θ and the Koopman matrices A and B are learned end-to-end. The trainable parameters are $\mathcal{T} \doteq (\theta, \mathbf{A}, \mathbf{B})$.

III. THEORETICAL ANALYSIS OF SCALING LAW

We establish the theoretical foundations of neural Koopman scaling laws. While prior works establish the asymptotic convergence of data-driven algorithms like Extended Dynamic Mode Decomposition (EDMD) to the true operator \mathcal{K} as sample size $m \rightarrow \infty$ and latent dimension $n \rightarrow \infty$ [20], [32], [33], Our analysis builds upon these foundational results but differs by providing **explicit convergence rates** under additional well-defined assumptions. For clarity, we analyze autonomous systems, which naturally extend to controlled systems via the augmented state $s = [x^\top, u^\top]^\top$.

A. Error Decomposition

1) *Koopman Operator Theory*: Consider a discrete-time dynamical system $s^+ = f(s)$ on a separable topological space \mathcal{S} with invariant measure μ . We lift the analysis to the space of observables $\mathcal{H} \subset L_2(\mathcal{S}, \mu)$, the separable Hilbert space of square-integrable functions. This construction serves two purposes: first, the separability of \mathcal{H} ensures a countable orthonormal basis for finite-dimensional truncation; second, the invariance of μ allows invoking Birkhoff's Ergodic Theorem [34] to approximate ensemble averages via single time trajectories. The inner product on \mathcal{H} is defined as:

$$\langle g_1, g_2 \rangle_{\mathcal{H}} := \int_{\mathcal{S}} g_1(s) g_2^*(s) d\mu(s) \quad (7)$$

The **Koopman operator** $\mathcal{K} : \mathcal{H} \rightarrow \mathcal{H}$ acts on any $\psi \in \mathcal{H}$ via:

$$(\mathcal{K}\psi)(s) = \psi \circ f(s) \quad (8)$$

2) EDMD (Extended Dynamic Mode Decomposition):

EDMD finds a finite-dimensional matrix approximation of the Koopman operator \mathcal{K} . Given an embedding $\Phi(s) = [\phi_1(s), \dots, \phi_n(s)]^\top \in \mathbb{R}^n$, we define the latent subspace $\mathcal{H}_n = \text{span}\{\phi_1, \dots, \phi_n\}$. For m data pairs $\{(s_i, s_i^+)\}_{i=1}^m$, EDMD seeks a matrix $\mathbf{K}_{n,m} \in \mathbb{R}^{n \times n}$ that minimizes the empirical squared error:

$$\min_{\mathbf{K} \in \mathbb{R}^{n \times n}} \sum_{i=1}^m \|\Phi(s_i^+) - \mathbf{K}\Phi(s_i)\|_2^2 \quad (9)$$

where $\|\cdot\|_2$ is the Euclidean norm. While this objective generalizes to l_p norms, we restrict our analysis to l_2 to leverage spectral properties. Assuming the empirical Gram matrix $\mathbf{G}_{n,m}$ is invertible, this yields the closed-form solution:

$$\mathbf{K}_{n,m} = \mathbf{A}_{n,m} \mathbf{G}_{n,m}^{-1}, \quad (10)$$

$$\mathbf{G}_{n,m} = \frac{1}{m} \sum_{i=1}^m \Phi(s_i) \Phi(s_i)^\top, \quad \mathbf{A}_{n,m} = \frac{1}{m} \sum_{i=1}^m \Phi(s_i^+) \Phi(s_i)^\top.$$

In the infinite-data limit ($m \rightarrow \infty$), we define the population Gram matrix \mathbf{G}_n and correlation matrix \mathbf{A}_n via expectations

over the invariant measure μ , yielding the ideal finite-rank operator \mathbf{K}_n :

$$\mathbf{K}_n = \mathbf{A}_n \mathbf{G}_n^{-1} \quad (11)$$

$$\mathbf{G}_n = \mathbb{E}_s[\Phi(s)\Phi(s)^\top], \quad \mathbf{A}_n = \mathbb{E}_s[\Phi(s^+)\Phi(s)^\top].$$

Here, \mathbf{K}_n represents the optimal projection of \mathcal{K} onto \mathcal{H}_n given perfect distributional knowledge, serving as the noise-free limit of the empirical estimator $\mathbf{K}_{n,m}$.

3) *Koopman Approximation Error*: A key insight from [33] is that EDMD approximates the Koopman operator \mathcal{K} via an orthogonal projection onto \mathcal{H}_n . We distinguish the *empirical projection* $\mathcal{K}_{n,m}$, which minimizes empirical risk over m samples, from the *ideal projection* \mathcal{K}_n , defined over the true measure μ as the population limit $\mathcal{K}_n = \lim_{m \rightarrow \infty} \mathcal{K}_{n,m}$.

We define the overall approximation error $\epsilon(n, m)$ as the distance between empirical operator $\mathcal{K}_{n,m}$ and infinite-dimensional operator \mathcal{K} in the induced operator norm $\|\cdot\|_{\mathcal{L}(\mathcal{H})}$:

$$\begin{aligned} \epsilon(n, m) &:= \|\mathcal{K}_{n,m} \mathcal{P}_n - \mathcal{K}\|_{\mathcal{L}(\mathcal{H})} \\ &= \sup_{\psi \in \mathcal{H}, \|\psi\|_{\mathcal{H}}=1} \|(\mathcal{K}_{n,m} \mathcal{P}_n - \mathcal{K})\psi\|_{\mathcal{H}}, \end{aligned} \quad (12)$$

where $\mathcal{P}_n : \mathcal{H} \rightarrow \mathcal{H}_n$ is the orthogonal subspace projection. Using \mathcal{K}_n as an intermediate reference, the triangle inequality yields:

$$\epsilon(n, m) \leq \underbrace{\|\mathcal{K}_{n,m} \mathcal{P}_n - \mathcal{K}_n \mathcal{P}_n\|_{\mathcal{L}(\mathcal{H})}}_{\epsilon_{\text{samp}}(n, m)} + \underbrace{\|\mathcal{K}_n \mathcal{P}_n - \mathcal{K}\|_{\mathcal{L}(\mathcal{H})}}_{\epsilon_{\text{proj}}(n)}. \quad (13)$$

This separates the error into two sources. **1) Sampling Error** (ϵ_{samp}): The variance error arising from finite-sample estimation, quantifying the deviation of $\mathcal{K}_{n,m}$ from its population limit \mathcal{K}_n . **2) Projection Error** (ϵ_{proj}): The bias error representing the irreducible information loss caused by projecting the infinite-dimensional \mathcal{K} onto the finite n -dimensional subspace \mathcal{H}_n . While prior work established asymptotic convergence, our contribution derives explicit scaling rates for both ϵ_{samp} and ϵ_{proj} under assumptions relevant to neural embeddings.

B. Convergence of Sampling error

We establish the necessary assumptions for our analysis:

Assumption 1 (i.i.d. Samples). Data samples $\{(s_i, s_i^+)\}_{i=1}^m$ are drawn independently and identically from a distribution μ .

Assumption 2 (Bounded Latent State). The embedding is uniformly bounded. Specifically, there exists a constant $B > 0$ such that $\|\Phi(s)\|_2 \leq B$ for all $s \in \mathcal{S}$.

Assumption 3 (Well-Conditioned Gram Matrix). The infinite-data Gram matrix \mathbf{G}_n is strictly positive definite with $\lambda_{\min}(\mathbf{G}_n) \geq \gamma > 0$. We further assume that for a finite sample size m , the empirical Gram matrix $\mathbf{G}_{n,m}$ remains well-conditioned (specifically $\lambda_{\min}(\mathbf{G}_{n,m}) \geq \frac{\gamma}{2}$) with probability at least $1 - \delta_m$, where $\lim_{m \rightarrow \infty} \delta_m = 0$.

Assumption 1 can be relaxed to ergodic sampling, where time averages converge to ensemble averages [33]. Assumption 2 is easily satisfied via bounded activations (e.g., \tanh) or weight normalization. Assumption 3 ensures the learned

embeddings are linearly independent in the population limit. While strictly positive, $\lambda_{\min}(\mathbf{G}_n)$ typically decreases as n grows due to latent ‘‘spectral crowding.’’ For finite samples, matrix concentration inequalities [35] guarantee that for sufficiently large m , $\mathbf{G}_{n,m}$ concentrates around \mathbf{G}_n , ensuring invertibility with high probability $1 - \delta_m$.

Proposition 1 (Sampling Error). *Under assumptions 1 to 3, with probability at least $1 - 2\delta - \delta_m$, the sampling error is bounded by:*

$$\epsilon_{\text{samp}}(n, m) \leq \kappa_{\text{bias}} \cdot \frac{\ln(2n/\delta)}{m} + \kappa_{\text{var}} \cdot \sqrt{\frac{\ln(2n/\delta)}{m}} \quad (14)$$

$$\kappa_{\text{bias}} = \frac{4B^3}{3\sqrt{\gamma^3}} \left(\frac{2B^2}{\gamma} + 1 \right), \kappa_{\text{var}} = \frac{2\sqrt{2}B^3}{\sqrt{\gamma^3}} \left(\frac{2B^2}{\gamma} + 1 \right)$$

Proof. In the data-driven framework, the finite-rank operator $\mathcal{K}_{n,m}$ is computationally realized by the matrix $\mathbf{K}_{n,m} \in \mathbb{R}^{n \times n}$. To rigorously analyze the approximation error, we must establish a link between the induced operator norm on the Hilbert space \mathcal{H} and a tractable matrix norm on the Euclidean space.

The sampling error operator, $(\mathcal{K}_{n,m} - \mathcal{K}_n)\mathcal{P}_n$, acts on functions in the subspace \mathcal{H}_n . Since every function $\psi \in \mathcal{H}_n$ is uniquely represented by a coefficient vector $\mathbf{c} \in \mathbb{R}^n$ (via $\psi = \mathbf{c}^\top \Phi$), the operator deviation corresponds directly to the matrix deviation $\Delta \mathbf{K} = \mathbf{K}_{n,m} - \mathbf{K}_n$. However, because the basis Φ is not necessarily orthonormal, the geometry of the Hilbert space is distorted relative to the Euclidean space. This distortion is captured by the population Gram matrix \mathbf{G}_n .

Under Assumption 2, the operator norm on $\mathcal{L}(\mathcal{H})$ is equivalent to a weighted matrix norm. Specifically, it is upper-bounded by the spectral norm of the matrix difference, scaled by the condition number of the basis geometry [23]. This relationship yields the following upper bound on the sampling error:

$$\begin{aligned} \epsilon_{\text{samp}} &= \|(\mathcal{K}_{n,m} - \mathcal{K}_n)\mathcal{P}_n\|_{\mathcal{L}(\mathcal{H})} = \|\mathbf{G}_n^{1/2}(\mathbf{K}_{n,m} - \mathbf{K}_n)\mathbf{G}_n^{-1/2}\|_{\sigma} \\ &\leq \sqrt{\kappa} \mathbf{G}_n \cdot \|\mathbf{K}_{n,m} - \mathbf{K}_n\|_{\sigma} \leq \sqrt{\kappa} \cdot \|\mathbf{K}_{n,m} - \mathbf{K}_n\|_{\sigma} \end{aligned} \quad (15)$$

where $\|\cdot\|_{\sigma}$ denotes the spectral norm of the coefficient matrices. The scalar pre-factor $\sqrt{\kappa} \mathbf{G}_n$ quantifies the geometric distortion induced by the feature basis, defined via the condition number of the Gram matrix \mathbf{G}_n . By applying assumption 2 and assumption 3, we derive a system-dependent constant upper bound κ for this condition number:

$$\kappa_{\mathbf{G}_n} := \frac{\lambda_{\max}(\mathbf{G}_n)}{\lambda_{\min}(\mathbf{G}_n)} \leq \frac{\mathbb{E}_s[\|\Phi(s)\|_2^2]}{\gamma} \leq \frac{B^2}{\gamma} := \kappa. \quad (16)$$

Remark 1. We emphasize that the upper bound κ derived in (16) is a system-dependent constant independent of the sample size m and latent dimension n , determined solely by the population geometry of the bounded feature basis. While strict orthonormality (assumption 4) represents the ideal case where $\mathbf{G}_n = \mathbf{I}$ (implying $\kappa = 1$), it is not a prerequisite for the convergence of the sampling error. This insight motivates the covariance regularization (\mathcal{L}_{cov}) to be introduced in section IV, which explicitly minimizes this constant by driving the learned basis towards orthonormality. By forcing the Gram

matrix closer to the identity, the regularization ensures the effective condition number approaches unity, thereby tightening the error bound.

Furthermore, when the Koopman matrix is estimated via the ordinary least-squares approach (10), we have

$$\begin{aligned} \epsilon_{\text{samp}}(n, m) &\leq \sqrt{\kappa} \|\mathbf{K}_{n,m} - \mathbf{K}_n\|_{\sigma} \\ &= \sqrt{\kappa} \|\mathbf{A}_{n,m} \mathbf{G}_{n,m}^{-1} - \mathbf{A}_n \mathbf{G}_n^{-1}\|_{\sigma} \end{aligned} \quad (17)$$

We decompose the sampling error in (17), using the triangle inequality:

$$\begin{aligned} \epsilon_{\text{samp}}(n, m) &\leq \sqrt{\kappa} \|(\mathbf{A}_{n,m} - \mathbf{A}_n) \mathbf{G}_{n,m}^{-1} + \mathbf{A}_{n,m} (\mathbf{G}_{n,m}^{-1} - \mathbf{G}_n^{-1})\|_{\sigma} \\ &\leq \sqrt{\kappa} \|\mathbf{A}_{n,m} - \mathbf{A}_n\|_{\sigma} \|\mathbf{G}_{n,m}^{-1}\|_{\sigma} + \sqrt{\kappa} \|\mathbf{A}_{n,m}\|_{\sigma} \|\mathbf{G}_{n,m}^{-1} - \mathbf{G}_n^{-1}\|_{\sigma} \end{aligned} \quad (18)$$

To bound each term in (18), we utilize properties of matrix norms. First, we consider the difference of the inverses of $\mathbf{G}_{n,m}$ and \mathbf{G}_n . Using the identity $\mathbf{G}_{n,m}^{-1} - \mathbf{G}_n^{-1} = \mathbf{G}_n^{-1}(\mathbf{G}_n - \mathbf{G}_{n,m})\mathbf{G}_{n,m}^{-1}$, we have:

$$\|\mathbf{G}_{n,m}^{-1} - \mathbf{G}_n^{-1}\|_{\sigma} \leq \|\mathbf{G}_n^{-1}\|_{\sigma} \|\mathbf{G}_n - \mathbf{G}_{n,m}\|_{\sigma} \|\mathbf{G}_{n,m}^{-1}\|_{\sigma} \quad (19)$$

Based on Assumption 2, the spectral norm of $\mathbf{A}_{n,m}$ can be bounded:

$$\|\mathbf{A}_{n,m}\|_{\sigma} \leq \frac{1}{m} \sum_{i=1}^m \|\Phi(s_i)\|_2 \|\Phi(s_i^+)\|_2 \leq B^2 \quad (20)$$

The population bound follows directly from the strict positive definiteness in assumption 3: $\|\mathbf{G}_n^{-1}\|_{\sigma} \leq 1/\gamma$. For the empirical estimator, we invoke the finite-sample condition of assumption 3, which guarantees that the event $\mathcal{E}_{\text{inv}} = \{\lambda_{\min}(\mathbf{G}_{n,m}) \geq \gamma/2\}$ occurs with probability at least $1 - \delta_m$. Conditioned on \mathcal{E}_{inv} , the spectral norm of the empirical inverse is bounded by:

$$\|\mathbf{G}_{n,m}^{-1}\|_{\sigma} = \frac{1}{\lambda_{\min}(\mathbf{G}_{n,m})} \leq \frac{2}{\gamma}, \quad \|\mathbf{G}_n^{-1}\|_{\sigma} \leq \frac{1}{\gamma} \quad (21)$$

Substituting (19), (20), and (21) back into (18), with probability at least $1 - \delta_m$:

$$\epsilon_{\text{samp}}(n, m) \leq \frac{2B^2 \sqrt{\kappa}}{\gamma^2} \|\mathbf{G}_{n,m} - \mathbf{G}_n\|_{\sigma} + \frac{\sqrt{\kappa}}{\gamma} \|\mathbf{A}_{n,m} - \mathbf{A}_n\|_{\sigma} \quad (22)$$

To bound $\|\mathbf{G}_{n,m} - \mathbf{G}_n\|_{\sigma}$ and $\|\mathbf{A}_{n,m} - \mathbf{A}_n\|_{\sigma}$, we utilize the following lemma.

Lemma 1 (Matrix Bernstein Inequality [36]). *Let $\{Y_i\}_{i=1}^m$ be independent, mean-zero random matrices with dimensions $d_1 \times d_2$. Assume that each matrix satisfies $\|Y_i\|_{\sigma} \leq L$ almost surely. Define the variance parameter $v^2 = \|\sum_{i=1}^m \mathbb{E}[Y_i Y_i^\top]\|_{\sigma}$. Then, for all $\epsilon \geq 0$,*

$$\mathbb{P} \left(\left\| \sum_{i=1}^m Y_i \right\|_{\sigma} \geq \epsilon \right) \leq (d_1 + d_2) \exp \left(\frac{-\epsilon^2/2}{v^2 + L\epsilon/3} \right). \quad (23)$$

Let \mathbf{Y}_i be a sequence of zero-mean random matrices defined as:

$$\mathbf{Y}_i = \frac{1}{m} \{ \Phi(s_i) \Phi(s_i^+)^\top - \mathbb{E}[\Phi(s_i) \Phi(s_i^+)^\top] \} \quad (24)$$

It follows that $\mathbf{A}_{n,m} - \mathbf{A}_n = \sum_{i=1}^m \mathbf{Y}_i$. Note that independence of \mathbf{Y}_i follows directly from Assumption 1. Since each \mathbf{Y}_i is constructed solely from the i -th data pair, the sequence

$\{\mathbf{Y}_i\}_{i=1}^m$ is independent. Under Assumption 2, the norm of each \mathbf{Y}_i is bounded:

$$\|\mathbf{Y}_i\|_\sigma \leq \frac{1}{m} (\|\Phi(s_i)\Phi(s_i^+)^\top\|_\sigma + \|\mathbb{E}[\cdot]\|_\sigma) \leq \frac{2B^2}{m} \quad (25)$$

The variance parameter v^2 is bounded as $v^2 = \|\sum_{i=1}^m \mathbb{E}[\mathbf{Y}_i \mathbf{Y}_i^\top]\|_\sigma \leq \sum_{i=1}^m \|\mathbb{E}[\mathbf{Y}_i \mathbf{Y}_i^\top]\|_\sigma \leq \sum_{i=1}^m \mathbb{E}[\|\mathbf{Y}_i\|^2] \leq \sum_{i=1}^m \left(\frac{2B^2}{m}\right)^2 = \frac{4B^4}{m}$. Applying the Matrix Bernstein Inequality with $d_1 = d_2 = n$, $L = \frac{2B^2}{m}$, and $v^2 = \frac{4B^4}{m}$, we obtain: $\mathbb{P}(\|\mathbf{A}_{n,m} - \mathbf{A}_n\|_\sigma \geq \epsilon) = \mathbb{P}(\|\sum_{i=1}^m \mathbf{Y}_i\|_\sigma \geq \epsilon) \leq 2n \exp\left(\frac{-\epsilon^2/2}{4B^4/m + (2B^2/m)\epsilon/3}\right) = 2n \exp\left(\frac{-m\epsilon^2}{8B^4 + 4B^2\epsilon/3}\right)$. To guarantee this probability is at most δ , we equate the RHS (Right-Hand Side) to δ and solve for ϵ . Let $\tau = \ln(2n/\delta)$. The condition becomes: $\frac{m\epsilon^2}{8B^4 + 4B^2\epsilon/3} \geq \tau \implies m\epsilon^2 - \frac{4}{3}B^2\tau\epsilon - 8B^4\tau \geq 0$. This is a quadratic inequality in ϵ . The critical value is the positive root of the corresponding equation:

$$\epsilon = \frac{\frac{4}{3}B^2\tau + \sqrt{\frac{16}{9}B^4\tau^2 + 32mB^4\tau}}{2m} \quad (26)$$

Using the sub-additivity of the square root, $\sqrt{x+y} \leq \sqrt{x} + \sqrt{y}$, we simplify the upper bound $\epsilon \leq \frac{2B^2\tau}{3m} + \sqrt{\frac{16}{9}B^4\tau^2 + \frac{32mB^4\tau}{2m}} = \frac{2B^2\tau}{3m} + \frac{2B^2\tau}{3m} + \sqrt{\frac{8B^4\tau}{m}} = \frac{4B^2\tau}{3m} + \sqrt{\frac{8B^4\tau}{m}}$. Substituting $\tau = \ln(2n/\delta)$ into the derived solution yields the explicit non-asymptotic bound holding with probability at least $1 - \delta$:

$$\|\mathbf{A}_{n,m} - \mathbf{A}_n\|_\sigma \leq \frac{4B^2 \ln(2n/\delta)}{3m} + \sqrt{\frac{8B^4 \ln(2n/\delta)}{m}} \quad (27)$$

An identical concentration argument applies to the Gram matrix approximation error $\|\mathbf{G}_{n,m} - \mathbf{G}_n\|_\sigma$, as it satisfies the same spectral and variance bounds under Assumption 2. Thus, with probability at least $1 - \delta$:

$$\|\mathbf{G}_{n,m} - \mathbf{G}_n\|_\sigma \leq \frac{4B^2 \ln(2n/\delta)}{3m} + \sqrt{\frac{8B^4 \ln(2n/\delta)}{m}} \quad (28)$$

To bound the total sampling error ϵ_{samp} , we invoke a union bound. The intersection of the events in (27) and (28) holds with probability at least $1 - 2\delta$. Furthermore, the stability condition for the empirical Gram matrix inverse in (22) holds with probability at least $1 - \delta_m$. Substituting these bounds into (22) and factoring common terms, we obtain the following conclusion: (14) holds with probability at least $1 - 2\delta - \delta_m$, where $\kappa_{\text{bias}} = \frac{4B^2\sqrt{\kappa}}{3} \left(\frac{2B^2}{\gamma^2} + \frac{1}{\gamma}\right)$, $\kappa_{\text{var}} = 2\sqrt{2}B^2\sqrt{\kappa} \left(\frac{2B^2}{\gamma^2} + \frac{1}{\gamma}\right)$. Using the definition of κ in (16), we prove proposition 1. ■ ■

For large sample sizes ($m \rightarrow \infty$), the error is dominated by the $\mathcal{O}(m^{-1/2})$ term. Treating the regularization and basis bounds as fixed, the asymptotic scaling with respect to sample size m and dimension n is:

$$\epsilon_{\text{samp}}(n, m) = \mathcal{O}\left(\sqrt{\frac{\ln(n)}{m}}\right) \quad (29)$$

This scaling implies a requisite sample complexity to maintain approximation fidelity as the model dimension grows.

specifically, if the sample size scales super-linearly as $m \propto n \ln(n)$, the sampling error vanishes with respect to the model dimension n :

$$\epsilon_{\text{samp}}(n, m) \Big|_{m \propto n \ln(n)} = \mathcal{O}\left(\sqrt{\frac{\ln n}{n \ln n}}\right) = \mathcal{O}\left(\frac{1}{\sqrt{n}}\right) \quad (30)$$

This result confirms that increasing the latent dimension n improves the operator approximation, provided the data volume m scales appropriately ($m \gtrsim n \ln n$).

C. Convergence of Projection Error

In this section, we establish the convergence of the projection error $\epsilon_{\text{proj}}(n)$ as the dimension n of the latent subspace \mathcal{H}_n increases. This requires a different set of assumptions from the sampling error.

Assumption 4 (Orthogonal basis). The embedding functions $\{\phi_i\}_{i=1}^n$ that span \mathcal{H}_n form an orthonormal set with respect to the inner product on \mathcal{H} . In matrix notation, this implies that the population Gram matrix is exactly the identity matrix, i.e., $\langle \phi_i, \phi_j \rangle_{\mathcal{H}} = 0$ for $i \neq j$ and 1 for $i = j$.

Assumption 5 (Bounded Koopman Operator). The Koopman operator $\mathcal{K} : \mathcal{H} \rightarrow \mathcal{H}$ is bounded, i.e. $\|\mathcal{K}\|_\sigma \leq M < \infty$.

Assumption 6 (Spectral Decay). The eigenvalues of the Koopman operator \mathcal{K} , sorted by magnitude as $|\lambda_1^*| \geq |\lambda_2^*| \geq \dots$, decay at least at a polynomial rate: $|\lambda_i^*| \leq \frac{C}{i^\alpha}$ for some constant $C > 0, \alpha > \frac{1}{2}$.

Assumption 7 (Subspace Approximation Capability). Let $\mathcal{H}_n^* = \text{span}\{\phi_1^*, \dots, \phi_n^*\}$ be the subspace spanned by the n dominant eigenfunctions of \mathcal{K} . We assume the hypothesis class of the neural network Φ_θ is sufficiently expressive such that there exists a parameter setting θ^* where the learned subspace \mathcal{H}_n aligns with \mathcal{H}_n^* .

Assumption 4 is nonrestrictive since any countable dense subset of \mathcal{H} can be orthonormalized using the Gram-Schmidt process. Assumption 5 holds, for instance, when the system dynamics are Lipschitz continuous and the state space is bounded. Assumption 6 holds for many stable physical systems that dissipate energy. Assumption 7 implies that our neural network's optimization has learned the most dominant modes of the system dynamics, which is reasonable given the universal approximation capabilities of neural networks and the optimization objective in (9).

Proposition 2 (Projection Error). *Under assumptions 4 to 7, the project error satisfies:*

$$\epsilon_{\text{proj}}(n) \leq \frac{C}{\sqrt{2\alpha - 1}} \cdot \frac{1}{n^{\alpha-1/2}} \quad (31)$$

Proof. The projection error ϵ_{proj} is the irreducible approximation bias from truncating \mathcal{K} to rank n :

$$\epsilon_{\text{proj}} = \|\mathcal{K}_n \mathcal{P}_n - \mathcal{K}\|_{\mathcal{L}(\mathcal{H})} \quad (32)$$

To rigorously quantify the projection error, we begin with the definition of the induced operator norm on \mathcal{H} . The error $\epsilon_{\text{proj}}(n)$ is defined as the supremum of the approximation

residual over the unit ball:

$$\epsilon_{\text{proj}}(n) = \sup_{\psi \in \mathcal{H}, \|\psi\|_{\mathcal{H}}=1} \|(\mathcal{K}_n \mathcal{P}_n - \mathcal{K})\psi\|_{\mathcal{H}} \quad (33)$$

Under Assumption 4, the space \mathcal{H} admits an orthonormal eigenbasis $\{\phi_i\}_{i=1}^{\infty}$ with corresponding eigenvalues λ_i . Any unit-norm function ψ can be expanded as $\psi = \sum_{i=1}^{\infty} c_i \phi_i$, where the coefficients satisfy $\sum_{i=1}^{\infty} |c_i|^2 = 1$.

We analyze the action of the error operator on ψ . Invoking Assumption 7, we note that the finite-rank operator \mathcal{K}_n accurately captures the first n eigenvalues (i.e., $\mathcal{K}_n \phi_i = \lambda_i \phi_i$ for $i \leq n$) and that \mathcal{P}_n is an orthogonal projection onto $\text{span}\{\phi_1, \dots, \phi_n\}$. The error expansion proceeds as $(\mathcal{K}_n \mathcal{P}_n - \mathcal{K})\psi = \mathcal{K}_n \mathcal{P}_n (\sum_{i=1}^{\infty} c_i \phi_i) - \mathcal{K} (\sum_{i=1}^{\infty} c_i \phi_i) = \mathcal{K}_n (\sum_{i=1}^n c_i \phi_i) - \sum_{i=1}^{\infty} c_i \lambda_i \phi_i = \sum_{i=1}^n c_i \lambda_i \phi_i - (\sum_{i=1}^n c_i \lambda_i \phi_i + \sum_{i=n+1}^{\infty} c_i \lambda_i \phi_i) = -\sum_{i=n+1}^{\infty} c_i \lambda_i \phi_i$. The squared norm of this residual is determined by the energy of the truncated modes. Utilizing the orthonormality of the basis $\{\phi_i\}$, we have:

$$\|(\mathcal{K}_n \mathcal{P}_n - \mathcal{K})\psi\|_{\mathcal{H}}^2 = \left\| \sum_{i=n+1}^{\infty} c_i \lambda_i \phi_i \right\|_{\mathcal{H}}^2 = \sum_{i=n+1}^{\infty} |c_i|^2 |\lambda_i|^2 \quad (34)$$

The operator norm is the supremum of this quantity subject to $\sum |c_i|^2 = 1$, which implies that $|c_i|^2 \leq 1$ for all i . While the exact operator norm corresponds to the spectral radius of the tail ($\sup_{i>n} |\lambda_i|$), we seek a bound in terms of the aggregate spectral energy to characterize the total information loss. We can thus bound the error:

$$\epsilon_{\text{proj}}(n)^2 = \sup_{\|c\|=1} \sum_{i=n+1}^{\infty} |c_i|^2 |\lambda_i|^2 \leq \sum_{i=n+1}^{\infty} |\lambda_i|^2 \quad (35)$$

Considering Assumption 6, the singular values satisfy the polynomial decay bound $\lambda_i^* \leq C/i^\alpha$ and $\alpha > 1/2$. To upper-bound the tail sum of the squared singular values, we employ the Integral Test for series convergence [37]. Since the function $f(x) = x^{-2\alpha}$ is positive and monotonically decreasing on $x \in [n, \infty)$, the sum is bounded by the corresponding integral, given that $\epsilon_{\text{proj}}(n)^2 \leq \sum_{i=n+1}^{\infty} \left(\frac{C}{i^\alpha}\right)^2 = C^2 \sum_{i=n+1}^{\infty} \frac{1}{i^{2\alpha}} \leq C^2 \int_n^{\infty} \frac{1}{x^{2\alpha}} dx = C^2 \left[\frac{x^{1-2\alpha}}{1-2\alpha} \right]_n^{\infty} = C^2 \left(0 - \frac{n^{1-2\alpha}}{1-2\alpha}\right) = \frac{C^2}{2\alpha-1} n^{1-2\alpha}$. Taking the square root of both sides, we obtain the final convergence rate in (31). ■ ■

This result establishes the asymptotic scaling law for the projection error with respect to the latent dimension n :

$$\epsilon_{\text{proj}}(n) = \mathcal{O}\left(\frac{1}{n^{\alpha-\frac{1}{2}}}\right) \quad (36)$$

In the specific case where the spectrum decays harmonically ($\alpha = 1$), we recover the standard slow rate:

$$\epsilon_{\text{proj}}(n) = \mathcal{O}\left(\frac{1}{\sqrt{n}}\right) \quad (37)$$

Thus, the projection error is guaranteed to vanish as the latent dimension increases, provided the system dynamics exhibit sufficient spectral decay.

D. Convergence of Koopman Operator

We now synthesize the results from the sampling and projection analyses to establish the fundamental scaling law of Neural Koopman operators.

Theorem 1 (Error Bound). *Consider the problem of approximating the true Koopman operator \mathcal{K} using a finite dataset of size m projected onto an n -dimensional latent subspace using Neural Networks. Under assumptions 1 to 7, with probability at least $1 - 2\delta - \delta_m$, the total approximation error is bounded by the sum of the sampling and projection errors:*

$$\epsilon(n, m) \leq \underbrace{\frac{\kappa_{\text{bias}} \ln(2n/\delta)}{m} + \kappa_{\text{var}} \sqrt{\frac{\ln(2n/\delta)}{m}}}_{\epsilon_{\text{samp}}(n, m)} + \underbrace{\frac{C}{\sqrt{2\alpha-1}} n^{-(\alpha-1/2)}}_{\epsilon_{\text{proj}}(n)} \quad (38)$$

The proof of the theorem follows easily from the two propositions discussed earlier. Based on this non-asymptotic bound, we derive the asymptotic scaling behavior and the convergence conditions.

Corollary 1 (Scaling Law). *Under assumptions 1 to 7, in the asymptotic regime where sample size $m \rightarrow \infty$ and latent dimension $n \rightarrow \infty$, the error scaling follows the power law:*

$$\epsilon(n, m) = \mathcal{O}\left(\sqrt{\frac{\ln n}{m}}\right) + \mathcal{O}\left(\frac{1}{n^{\alpha-\frac{1}{2}}}\right) \quad (39)$$

Theorem 1 establishes the scaling law and an explicit upper bound on the approximation error of Koopman operators. By relaxing assumptions 4, 6 and 7, the following corollary extends this result and guarantees consistency under weaker, more practical conditions.

Corollary 2 (Asymptotic Convergence). *Consider the learned Koopman operator $K_{n,m}$ under Assumptions 1–3 (Well-conditioned Sampling) and Assumption 5 (Bounded Operator). Suppose further that the class of neural network embedding functions Φ_θ satisfies the Universal Approximation Property (i.e., the union of the spanned subspaces is dense in \mathcal{H} as $n \rightarrow \infty$).*

Then, the estimator converges to the true Koopman operator \mathcal{K} in the strong operator topology:

$$\lim_{n \rightarrow \infty} \lim_{m = \Omega(n \ln n)} \|K_{n,m} \mathcal{P}_n - \mathcal{K}\|_{\mathcal{L}(\mathcal{H})} = 0. \quad (40)$$

Proof. The proof follows the error decomposition structure established in (13), but diverges in the analysis of the projection term by relaxing the structural assumptions.

Convergence of Sampling Error (Limit on m). The analysis for the sampling error directly follows the concentration arguments in proposition 1. Under assumptions 1 to 3, the empirical estimators converge to their population counterparts. Specifically, provided the sample size scales super-linearly with dimension ($m = \Omega(n \ln n)$), the sampling error decreases:

$$\lim_{m \rightarrow \infty} \lim_{m = \Omega(n \ln n)} \epsilon_{\text{samp}}(n, m) = 0. \quad (41)$$

Convergence of Projection Error (Limit on n). For the projection error, we relax the strict structural constraints imposed by assumption 6 and assumption 7. We replace these with

the standard *Universal Approximation Property* of deep neural networks [38], [39].

The Universal Approximation Theorem guarantees that standard feedforward networks are dense in the space of continuous functions over compact domains. In our context, this implies that for any observable function $\psi \in \mathcal{H}$ and any error tolerance $\epsilon > 0$, there exists a parameter set θ such that the learned embedding subspace $\mathcal{H}_n = \text{span}(\Phi_\theta)$ satisfies:

$$\inf_{\phi_\theta \in \mathcal{H}_n} \|\psi - \phi_\theta\|_{\mathcal{H}} < \epsilon. \quad (42)$$

Mathematically, this property ensures that the sequence of learned subspaces $\{\mathcal{H}_n\}$ becomes dense in the Hilbert space \mathcal{H} as the network width increases (i.e., $\overline{\cup_n \mathcal{H}_n} = \mathcal{H}$). By the projection theorem, if the subspace sequence is dense, the associated orthogonal projection operators \mathcal{P}_n converge strongly to the identity operator \mathcal{I} . Consequently, the projection bias for any bounded Koopman operator \mathcal{K} vanishes in the limit:

$$\begin{aligned} \lim_{n \rightarrow \infty} \epsilon_{\text{proj}}(n) &= \lim_{n \rightarrow \infty} \|(\mathcal{K}\mathcal{P}_n - \mathcal{K})\|_{\mathcal{L}(\mathcal{H})} \\ &\leq \|\mathcal{K}\|_{\mathcal{L}(\mathcal{H})} \cdot \lim_{n \rightarrow \infty} \|\mathcal{P}_n - \mathcal{I}\|_{\mathcal{L}(\mathcal{H})} = 0. \end{aligned} \quad (43)$$

■

■

Remark 2 (Assumption Strength). The condition of Universal Approximation Property is significantly weaker than the previous assumptions. Assumption 6 dictates a specific *rate* of information decay, and Assumption 7 assumes the optimizer successfully locates the *optimal* invariant subspace. In contrast, the Universal Approximation Property asserts only that the neural network has the *capacity* to approximate any square-integrable function to arbitrary precision as the latent dimension $n \rightarrow \infty$. It provides an existence guarantee rather than a rate guarantee.

Remark 3 (Comparison with Prior Work). Unlike foundational analyses of EDMD such as Korda and Mezić [33], which primarily establish *asymptotic* consistency: guaranteeing that the estimator converges to the true operator in the limit of infinite data ($m \rightarrow \infty$) and infinite model capacity ($n \rightarrow \infty$), Theorem 1 derives explicit *non-asymptotic* error bounds. By characterizing the exact decay rates of the sampling error and projection error as functions of finite resources, we provide a rigorous theoretical justification for the ‘‘Scaling Laws’’ observed in neural Koopman models. Furthermore, our analysis yields specific design insights absent in asymptotic proofs: first, we identify the requisite sample complexity ($m = \Omega(n \ln n)$) needed to suppress the variance of high-dimensional embeddings; second, our bound explicitly captures the role of the basis conditioning constant (γ), thereby providing a theoretical motivation for the covariance regularization (\mathcal{L}_{cov}) introduced in section IV to stabilize learning.

E. More discussion about the assumptions

1) *Assumption 6: Spectral Decay*: Assumption 6 states that the Koopman eigenvalues $|\lambda_j^*|$, when ordered by magnitude, decay at a rate bounded by a polynomial, $|\lambda_i^*| \leq C/i^\alpha$. This condition is not merely a convenience for bounding the projection error; it is a structural consequence of the dynamical flow’s regularity. Classical control theory establishes that for

systems evolving on compact attractors with differentiable dynamics, the spectral coefficients decay algebraically (or exponentially for analytic dynamics) [40], [41]. Consequently, the operator is effectively low-rank: the system’s energy concentrates within a finite set of dominant modes, while the spectral tail vanishes rapidly.

This spectral decay is also essential from a perturbation-theoretic perspective. In robotics, measurement noise can produce high-frequency modes, leading to spectral pollution, where small eigenvalues are identified as artifacts of noise rather than true system dynamics. Assumption 6 ensures that the true spectral tail falls below the noise floor and can therefore be safely neglected. As a result, finite-dimensional projections (e.g., EDMD) converge to the true operator without losing significant dynamical information, even in the presence of noisy measurements.

2) *Assumption 7: Subspace Approximation Capability*: We assume that the learned embedding Φ_θ spans a subspace \mathcal{H}_n that approximates the dominant n -dimensional invariant subspace of the Koopman operator \mathcal{K} . This assumption bridges the gap between the optimization landscape and spectral theory.

Optimal Finite-Dimensional Approximation. The standard training objective minimizes the prediction error in the embedding space:

$$\mathcal{L}(\theta, \mathbf{K}) = \mathbb{E}_{s \sim \mu} \left[\|\Phi_\theta(s^+) - \mathbf{K}\Phi_\theta(s)\|_2^2 \right]. \quad (44)$$

For a fixed subspace \mathcal{H}_n , the optimal matrix \mathbf{K} is simply the Galerkin projection of \mathcal{K} onto \mathcal{H}_n . However, when optimizing over the embedding parameters θ simultaneously, the problem becomes a variational search for the optimal observation subspace.

The resulting approximation error is fundamentally governed by how well the chosen subspace \mathcal{H}_n aligns with the spectral structure of the Koopman operator \mathcal{K} . The optimal rank- n approximation, denoted as \mathcal{K}_n , is obtained by spectrally truncating \mathcal{K} onto its dominant n -dimensional invariant subspace: $\mathcal{H}_n^* = \text{span}\{\phi_1^*, \dots, \phi_n^*\}$. Where $\{\phi_i^*\}$ are Koopman eigenfunctions associated with the n eigenvalues of largest magnitude, $|\lambda_1^*| \geq \dots \geq |\lambda_n^*|$. Among all n -dimensional subspaces, the operator-norm approximation error is minimized when the learned embedding subspace $\mathcal{H}_n = \text{span}(\Phi_\theta)$ coincides with the true dominant eigenspace \mathcal{H}_n^* [17], [33]. Thus, the global minimum of the loss function $\mathcal{L}(\theta, \mathbf{K})$ is attained if and only if the learned embedding satisfies: $\text{span}(\Phi_\theta) \approx \mathcal{H}_n^*$.

Practical Realization via Deep Learning. Achieving this theoretical optimum in practice relies on two fundamental properties of the deep neural network parameterization Φ_θ . First, the Universal Approximation Theorem [38] guarantees that standard feedforward architectures are dense in the space of continuous functions. This ensures that the hypothesis class of the encoder Φ_θ is sufficiently rich to contain the optimal subspace \mathcal{H}_n^* . Specifically, given sufficient width, there exists a parameter configuration θ^* capable of approximating the true dominant eigenfunctions $\{\phi_i^*\}_{i=1}^n$ to arbitrary precision.

However, the existence of a solution does not guarantee its discovery. The simultaneous learning of the encoder parameters θ and the operator \mathbf{K} introduces a bilinear coupling, rendering the optimization landscape non-convex. While this

implies that convergence to the global optimum is not theoretically guaranteed, the search is favorably guided by the Spectral Bias (or Frequency Principle) inherent in gradient-based optimization [42]. Empirical and theoretical studies demonstrate that neural networks preferentially learn low-frequency, smooth components of a target function before fitting high-frequency details [42]. This intrinsic bias aligns naturally with our physical objective: dominant Koopman eigenfunctions associated with persistent dynamics typically exhibit high spatial regularity, whereas transient or noise-induced modes correspond to high-frequency spectral content [41]. Consequently, gradient-based training implicitly prioritizes robust, physically meaningful dynamics over transient or stochastic artifacts. This property is particularly advantageous for robotic system identification, where data are often limited and corrupted by measurement noise.

3) Optimization Error and the Scaling Floor: While the Universal Approximation Property guarantees the *existence* of parameters θ^* that recover the dominant invariant subspace \mathcal{H}_n^* (cf. assumption 7), it does not ensure that practical non-convex optimization procedures (e.g., stochastic gradient descent) will identify such parameters. In practice, optimization may converge only to a locally optimal representation. We therefore relax the strict requirement of exact subspace recovery imposed in assumption 7 and explicitly quantify the deviation from optimality.

Let \mathcal{P}_n denote the orthogonal projection onto the learned subspace $\mathcal{H}_n = \text{span}(\Phi_\theta)$, and let \mathcal{P}_n^* denote the projection onto the true dominant eigenspace \mathcal{H}_n^* . We define the *optimization residual* $\epsilon_{\text{opt}}(\theta)$, which measures the subspace misalignment between the learned representation and the optimal spectral subspace.

$$\epsilon_{\text{opt}}(\theta) \triangleq \|\mathcal{P}_n - \mathcal{P}_n^*\|_{\mathcal{L}(\mathcal{H})}. \quad (45)$$

Corollary 3 (Realizable Scaling Law). *Under assumptions 1 to 6, the total approximation error satisfies:*

$$\epsilon(n, m) \leq \underbrace{\mathcal{O}\left(\sqrt{\frac{\ln n}{m}}\right)}_{\text{sampling error}} + \underbrace{\mathcal{O}\left(n^{-(\alpha-1/2)}\right)}_{\text{projection error}} + \underbrace{\epsilon_{\text{opt}}(\theta)}_{\text{optimization error}} \quad (46)$$

The term $\epsilon_{\text{opt}}(\theta)$ encapsulates the algorithmic gap between the network's theoretical capacity and its realized performance. Unlike sampling and projection errors, which vanish asymptotically, ϵ_{opt} manifests as an *irreducible error floor* in the empirical scaling curves (see Fig. 2). As $m, n \rightarrow \infty$, the total error will saturate at this residual level unless the learned subspace closely aligns with \mathcal{H}_n^* .

IV. PRACTICAL NEURAL KOOPMAN OPERATORS

This section details our deep Koopman operator learning framework, including the model architecture, training objectives, data collection pipelines for various dynamical systems, and the evaluation protocol for both prediction and control tasks.

A. Koopman Model Architecture

Our model consists of an encoder network that lifts system states into a high-dimensional latent space where the dynamics are governed by a linear transition model. While the fundamental one-step transition map is often denoted as $z^+ = \mathbf{A}z + \mathbf{B}u$ as (4), we adopt the time-indexed notation z_t here to explicitly formulate the multi-step trajectory rollouts required for loss computation.

a) Encoder Network: Given a system state $x_t \in \mathbb{R}^{n_x}$, we employ a neural network $\Psi_\theta : \mathbb{R}^{n_x} \rightarrow \mathbb{R}^{n_{\text{enc}}}$ to extract higher-dimensional features. We then define the full embedding function $\Phi_\theta : \mathbb{R}^{n_x} \rightarrow \mathbb{R}^n$, which constructs the latent state z_t by concatenating the original state with these features:

$$z_t = \Phi_\theta(x_t) := [x_t, \Psi_\theta(x_t)] \in \mathbb{R}^n, \quad (47)$$

where $n = n_x + n_{\text{enc}}$ represents the total dimension of the latent space.

b) Latent Dynamics: The dynamics in the latent space are modeled by a discrete-time linear system with control u_t :

$$z_{t+1} = \mathbf{A}z_t + \mathbf{B}u_t, \quad (48)$$

where the matrices \mathbf{A} and \mathbf{B} are trainable, bias-free linear layers. To promote stable dynamics, the weight matrix \mathbf{A} is initialized to be near-orthogonal via Singular Value Decomposition (SVD), and the final layer of the encoder is initialized with orthogonal weights. This formulation models the control influence as a linear term in the latent space. While general Koopman theory allows for lifting the control input to capture non-affine dependencies (e.g., lifting u_t to u_t^2 or $x_t u_t$), we retain the explicit variable u_t without lifting. This design choice relies on the assumption that the underlying dynamics are control-affine (i.e., $x_{t+1} = f(x_t) + g(x_t)u_t$), which arises naturally from the Lagrangian mechanics of the robotic systems studied here. Furthermore, this linear-input structure ensures that the downstream MPC problem remains a convex Quadratic Program.

B. Training Objective

The model is trained end-to-end with a composite loss function designed to balance prediction accuracy, latent space structure, and control consistency:

$$\mathcal{L}_{\text{total}} = \mathcal{L}_{\text{pred}} + w_{\text{cov}} \mathcal{L}_{\text{cov}} + w_{\text{ctrl}} \mathcal{L}_{\text{ctrl}}, \quad (49)$$

where w_{cov} and w_{ctrl} are tunable scalar weights for the covariance and inverse dynamics losses, respectively.

a) Multi-Step Prediction Loss: To enforce temporal consistency, we unroll the learned Koopman dynamics forward from the encoded latent state z_t over a prediction horizon of T steps. Starting from $z_t = \Phi_\theta(x_t)$, the predicted latent states \hat{z}_τ for $\tau = t+1, \dots, t+T$ are generated recursively using the learned linear Koopman model:

$$\hat{z}_{\tau+1} = \mathbf{A}\hat{z}_\tau + \mathbf{B}u_\tau, \text{ for } \tau \geq t+1. \quad \hat{z}_t = z_t. \quad (50)$$

Each predicted latent state is mapped back to the state space via the projection operator \mathbf{P} , yielding the predicted physical state: $\hat{x}_\tau = \mathbf{P}\hat{z}_\tau$. The multi-step prediction loss penalizes the Mean Squared Error (MSE) between the predicted state \hat{x}_τ

and the corresponding ground-truth state x_τ :

$$\mathcal{L}_{\text{pred}} = \frac{1}{W} \sum_{\tau=t+1}^{t+T} \beta^{\tau-t} \|\hat{x}_\tau - x_\tau\|_2^2, \quad (51)$$

where $\beta \in (0, 1]$ is a temporal discount factor that emphasizes near-term prediction accuracy, and $W = \sum_{j=1}^T \beta^j$ is a normalization constant.

b) Covariance Loss.: To satisfy the conditioning requirement in assumption 4, the learned latent basis must remain well-conditioned and approximately linearly independent. We therefore explicitly regularize the covariance (empirical Gram) matrix of the latent features. Consistent with our theoretical notation, let $\Phi_\theta(s) \in \mathbb{R}^n$ be the embedding features of sample s . For a training batch of b samples $\{s_i\}_{i=1}^b$, we compute the empirical covariance matrix $\mathbf{G}_{\text{batch}} \in \mathbb{R}^{n \times n}$ as the centered finite-sample approximation of the Gram matrix:

$$\mathbf{G}_{\text{batch}} = \frac{1}{b-1} \sum_{i=1}^b (\Phi_\theta(s_i) - \bar{\Phi}_\theta)(\Phi_\theta(s_i) - \bar{\Phi}_\theta)^\top \quad (52)$$

where $\bar{\Phi}_\theta = \frac{1}{b} \sum_{i=1}^b \Phi_\theta(s_i)$ is the mean embedding vector. Recall that the sampling error bound in Proposition 1 depends inversely on γ , the minimum eigenvalue of the population Gram matrix (assumption 3). As the latent dimension n increases, the learned basis functions may become correlated, causing the smallest eigenvalue $\lambda_{\min}(\mathbf{G}_{\text{batch}})$ and consequently γ to approach zero, leading to ill-conditioning. To mitigate this effect, we introduce a covariance regularization term that penalizes off-diagonal entries of $\mathbf{G}_{\text{batch}}$:

$$\mathcal{L}_{\text{cov}} = \frac{1}{n(n-1)} \|\mathbf{G}_{\text{batch}} - \text{diag}(\mathbf{G}_{\text{batch}})\|_F^2. \quad (53)$$

By forcing off-diagonal terms toward zero, we encourage the learned basis to be orthogonal, ensuring $\lambda_{\min}(\mathbf{G}_{\text{batch}})$ and the related γ remain large even as model capacity increases. The normalization factor $n(n-1)$ equals the number of off-diagonal entries, so the loss represents the average squared off-diagonal magnitude. This scaling keeps gradient magnitudes approximately invariant to the latent dimension.

c) Inverse Control Loss.: While Koopman theory guarantees the existence of a linear controlled representation, the data-driven identification of the actuation matrix \mathbf{B} remains inherently ill-posed. Minimizing the forward prediction loss $\mathcal{L}_{\text{pred}}$ only constrains the composite transition (\mathbf{A}, \mathbf{B}) to match observed trajectories; it does not ensure that the control-to-latent mapping is injective. Consequently, degenerate solutions may arise in which \mathbf{B} is rank-deficient or poorly conditioned, causing distinct control inputs to induce nearly indistinguishable latent transitions. Such actuation ambiguity renders the downstream MPC problem ill-conditioned and potentially non-unique. This issue mirrors the conditioning requirement imposed in assumption 4, where the sampling error bound depends on the minimum eigenvalue of the Gram matrix. Analogously, reliable actuation recovery requires that \mathbf{B} have full column rank with $\lambda_{\min}(\mathbf{B}^\top \mathbf{B}) > 0$. Without this property, the control effect collapses into a low-energy subspace and violating identifiability.

To enforce actuation identifiability, we introduce an inverse dynamics loss. This acts as a regularization constraint

requiring that the control input u_τ be recoverable from the latent transition residual $(z_{\tau+1} - \mathbf{A}z_\tau)$. Recoverability of u_τ therefore requires \mathbf{B} to be well-conditioned. We estimate the control input via the least-squares pseudoinverse

$$\hat{u}_\tau = (\mathbf{B}^\top \mathbf{B})^\dagger \mathbf{B}^\top (z_{\tau+1} - \mathbf{A}z_\tau), \quad (54)$$

and the inverse loss penalizes the reconstruction error:

$$\mathcal{L}_{\text{ctrl}} = \frac{1}{W} \sum_{\tau=t}^{t+T-1} \beta^{\tau-t} \|\hat{u}_\tau - u_\tau\|_2^2. \quad (55)$$

As a result, the learned latent subspace not only predicts future states but faithfully captures the causal effect of actuation on system evolution. This structural consistency is essential for ensuring that the resulting MPC controller is well-posed, numerically stable, and uniquely responsive to control inputs.

C. Koopman-based Model Predictive Control

To evaluate the control performance of the learned operators, we embed them within a linear Model Predictive Control (MPC) framework. The learned Koopman model serves as the internal dynamics model. At each time step t , we solve a finite-horizon quadratic program (QP) to compute an optimal sequence of control inputs.

Unlike latent-space MPC formulations that penalize the full lifted state, we define the cost directly in the original (measurable) state space to prioritize physical tracking accuracy. Let x_τ denote the predicted physical state at time τ over a horizon of length H . The optimization problem is formulated as

$$\begin{aligned} \min_{\{u_\tau\}_{\tau=t}^{t+H-1}} & \sum_{\tau=t}^{t+H-1} (x_{\tau+1} - x_{\tau+1}^{\text{ref}})^\top Q (x_{\tau+1} - x_{\tau+1}^{\text{ref}}) + u_\tau^\top R u_\tau \\ \text{s.t.} & \quad z_{\tau+1} = \mathbf{A}z_\tau + \mathbf{B}u_\tau, \quad \tau = t, \dots, t+H-1, \\ & \quad u_{\min} \leq u_\tau \leq u_{\max}, \quad z_t = \Phi(x_t), \quad x_\tau = \mathbf{P}z_\tau. \end{aligned} \quad (56)$$

The learned linear dynamics evolve in the latent space, while physical states used in the objective are obtained through the projection mapping $x_\tau = \mathbf{P}z_\tau$. This formulation ensures that the controller optimizes performance in the true state space rather than regulating latent variables. At each time step, only the first control input u_t^* from the optimized sequence is applied to the system, and the procedure is repeated at the next step in a receding-horizon manner.

Following [25], we set $Q = I$ (consistent with the MSE-based training objective, without temporal discounting) and $R = 0$. This choice emphasizes physical tracking accuracy while not explicitly penalizing control effort. We leave joint design of the training loss and MPC cost as future work.

V. EXPERIMENTAL DESIGN

We empirically validate the theoretical convergence properties (Section III) by testing two hypotheses. **1) Robustness of Scaling Laws:** The theoretical power-law scaling of prediction error with dataset size (m) and latent dimension (n) holds empirically, even for complex robotic systems where spectral assumptions are only approximate. **2) Impact of Regularization:** Enforcing theoretical consistency via the proposed auxiliary losses (\mathcal{L}_{cov} and $\mathcal{L}_{\text{ctrl}}$) improves learning efficiency

and translates open-loop prediction gains into enhanced stability and tracking in closed-loop control. We validate these by analyzing prediction error scaling across varying data regimes and model sizes, followed by closed-loop control evaluations and ablations of the covariance and inverse losses.

A. Data Collection Strategy

To evaluate robustness across diverse dynamical systems, we adopt three data collection strategies:

Strategy I (Uniform State-Space Sampling): For stable synthetic systems, we uniformly sample initial states and control inputs to achieve broad, unbiased coverage of the global dynamics. **Strategy II (Randomized Simulation Actuation):** For simulated manipulators, we generate trajectories via randomized control (e.g., joint velocity commands), enabling diverse kinematic exploration without a predefined policy. **Strategy III (Constrained & Expert-Guided Exploration):** For physical hardware and unstable locomotion, where random actuation poses safety risks, we employ constrained optimization or aggregate expert demonstrations¹ with on-policy data to safely cover the necessary state distribution.

B. Experimental Setup

We validate our approach on seven dynamical systems of varying complexity, with state and control dimensions summarized in VI summarizes the dimensions for each environment used in the main experiment.

TABLE I: Summary of environment dimensions. Note: Unitree G1 and Go2 train on trimmed state-action spaces.

Environment	State Dim.	Action Dim.
Damping Pendulum	2	1
Double Pendulum	4	2
Franka Panda	14	7
Kinova Gen3	14	7
Unitree Go2	35	12
Unitree G1	53	23

Simulation experiment: For the Damping and Double Pendulums, we generate trajectories via uniform state-space sampling (Strategy I) with randomized control inputs. For the simulated 7-DoF Franka Panda manipulator, which includes internal low-level tracking dynamics that introduce realistic actuation discrepancies, we employ randomized joint velocity commands (Strategy II) from a nominal home configuration. To evaluate high-dimensional underactuated locomotion, we use the Unitree Go2 quadruped and G1 humanoid. Data is generated using expert-guided exploration (Strategy III), combining a pretrained RL expert policy with on-policy recovery data generated via Koopman-based MPC tracking.

Real-world experiment: We deploy our method on a physical Kinova Gen3 7-DoF manipulator. Because real-world data collection requires strict safety guarantees, we use Strategy III. We formulate a two-stage kinematic trajectory optimization procedure to compute feasible paths between random

¹Expert policies are utilized solely for safe data generation; the resulting Koopman model enables formal stability analysis and computationally efficient MPC that generalizes beyond the expert’s original objective .

configurations, followed by refinement to enforce collision avoidance and joint limits. Further evaluation details are in Supplementary Section 1.

C. Evaluation Metrics

We evaluate performance via *open-loop prediction accuracy* on held-out test sets and *closed-loop control*. Open-loop prediction error ($\mathcal{L}_{\text{pred}}$) is measured across all tasks to assess scaling and generalization, evaluating the learned dynamics independently of feedback. Tracking experiments focus on our most challenging high-dimensional platforms: the Franka arm and Unitree G1 and Go2 robots. For Franka, we report *End-Effector Tracking Error* on a figure-8 reference trajectory [43]. For G1 and Go2, we use *Mean Survival Steps* [25] to measure the average consecutive timesteps of successful locomotion tracking before violating safety limits (joint error > 0.10 rad for G1, > 0.16 rad for Go2). This metric directly captures closed-loop robustness in unstable, contact-rich regimes where small errors accumulate into catastrophic failures.

D. Model Architecture and Training Configuration

Architecture Details: While our framework is agnostic to network parameterization, we implement the encoder Ψ_θ as an MLP with two 256-unit hidden layers, ReLU activations, and residual connections to stabilize training.

Training Hyperparameters: To study scaling laws, we vary dataset sizes $m \in \{1000, 4000, 16000, 64000, 140000\}$ and scale the latent bottleneck via a multiplier $n_{\text{mult}} \in \{1, 2, 4, 8, 16\}$. Following (47), the encoder outputs $n_{\text{mult}} \times n_x$ nonlinear features. Concatenating these with the n_x -dimensional physical state x yields a total latent dimension $n = (n_{\text{mult}} + 1)n_x$. Each configuration is evaluated across five random seeds.

VI. EMPIRICAL ANALYSIS

A. Scaling Laws of Koopman Models

Our theoretical analysis (theorem 1 and corollary 3) decomposes the total approximation error into additive sampling (ϵ_{samp}) and projection (ϵ_{proj}) errors, plus an optimization residual. While corollary 3 implies latent dimension n couples projection bias and sampling variance, we empirically disentangle these via controlled experiments. We first isolate scaling behaviors for dataset size and dimension, deferring their combined interaction to section VI-A.3. To quantify these isolated effects, we fit the observed prediction error ϵ to a power-law:

$$\epsilon(D) = A \cdot D^{-\alpha} + C, \quad (57)$$

where D is the scaled resource (dataset m or dimension n), A is the decay magnitude, and C captures non-decaying errors. Mirroring the bound in corollary 3, when scaling samples ($D = m$) for fixed n , $Am^{-\alpha}$ models the decaying sampling error $\epsilon_{\text{samp}}(m)$. The constant C aggregates the m -invariant projection ($\epsilon_{\text{proj}}(n)$) and optimization (ϵ_{opt}) errors, representing the irreducible empirical error floor. Similarly, when scaling dimension ($D = n$) under fixed m , C encapsulates the sampling and optimization errors.

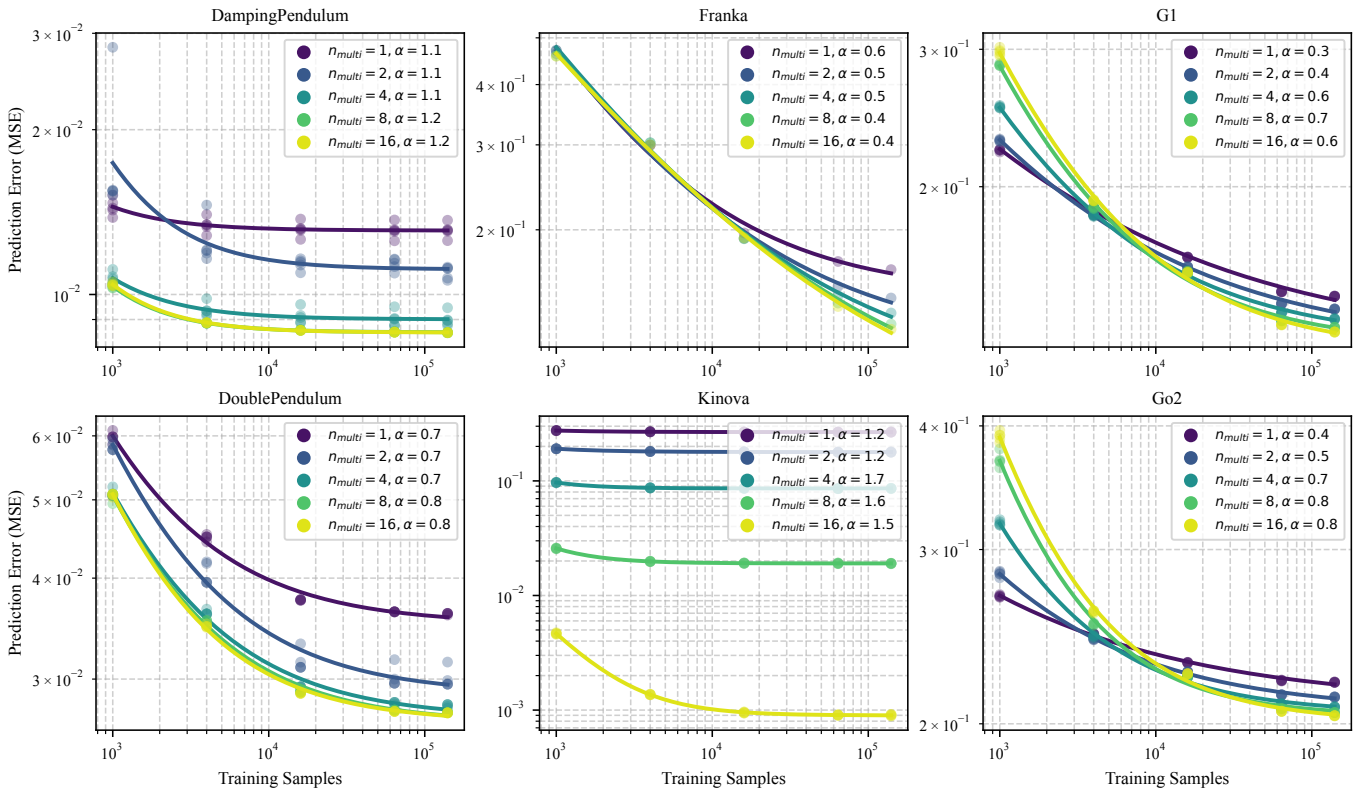


Fig. 2: Scaling of prediction error with training sample size (m). Subplots display error curves across latent dimension multipliers (n_{multi}). Dots denote random seeds, and solid lines show fitted power-law trends. The legend reports the scaling exponent α (error decay rate). Increasing dataset size consistently reduces error via a power law across environments, empirically validating theoretical sampling error convergence.

1) *Scaling with Training Sample Size*: This experiment empirically validates the sampling error bounds derived in proposition 1. Theoretically, this error scales as a sum of bias and variance components modulated by the subspace dimension n via the covering number factor $\ln(2n/\delta)$, taking the form in (14). To quantify this behavior, we fit the empirical prediction error to a power-law model $\epsilon(m) = Am^{-\alpha_m} + C$, where the decay rate α_m indicates sample efficiency and C represents the irreducible error floor from projection and optimization. Figure 2 confirms this power-law relationship, while the fitted exponents (table II) reveal three scaling regimes driven by data density, contact dynamics, and manifold complexity.

1) *Variance-Dominated Regime (Franka, G1, Go2)*: For high-dimensional systems with complex contact dynamics, sampling error decays slowly ($\alpha_m \in [0.49, 0.65]$), matching the theoretical 0.5 variance rate. Locomotion tasks involve sharp hybrid transitions (stick-slip friction) acting as high-frequency perturbations, requiring exponentially more data to resolve.

2) *Rapid Convergence Regime (Pendulums, Kinova)*: Systems with smoother intrinsic dynamics exhibit “fast-convergence” ($\alpha_m > 0.75$). Pendulums are analytically smooth and effectively low-rank. Interestingly, the Kinova dataset ($\alpha_m \approx 1.44$) relies on trajectory optimization, which confines data to a low-dimensional manifold of smooth, locally optimal paths, unlike the broad coverage of random exploration.

3) *Dimensionality Crossover (n vs. m)*: An explicit trade-off between capacity (n) and sample complexity (m) emerges

in the G1 and Go2 curves (fig. 2, Right). In the low-data regime ($m \approx 10^3$), expanding latent space causes overfitting because the variance component ($\propto \sqrt{\ln(n)/m}$) dominates. Conversely, with sufficient data ($m \approx 10^5$), variance is outweighed by the reduction in projection error (ϵ_{proj}), allowing larger models to outperform smaller ones (fig. 3).

TABLE II: Fitted power-law exponents (α) for prediction error decay. Sample efficiency α_m is averaged across latent dimensions and seeds. Spectral decay α_n is averaged across seeds in high-data regimes ($m \geq 10^4$), excluding smaller samples to isolate asymptotic projection error from finite-sample overfitting.

Environment	α_m (Sample Size)	α_n (Latent Dimension)
Damping Pendulum	1.15	4.3
Double Pendulum	0.75	2.89
Franka	0.49	1.16
Kinova	1.44	2.58
Go2	0.65	0.47
G1	0.52	0.34

2) *Scaling with Model Size*: We investigate the projection error decay versus latent dimension n . From proposition 2, this error is bounded by the Koopman spectrum’s tail energy, decaying polynomially via system structural regularity: $\epsilon_{\text{proj}} \lesssim \mathcal{O}(n^{-\alpha_n})$. Unlike sampling error decay ($\alpha_m \in [0.5, 1.0]$), the projection decay rate α_n varies significantly by environment, proxying the underlying dynamics’ *spectral complexity*. Fitting empirical data to $\epsilon(n) = An^{-\alpha_n} + C$, fig. 3 and table II reveal stark contrasts between simple and contact-rich environments.

1) *Fast Spectral Decay (Smooth Dynamics)*: Smooth, low-

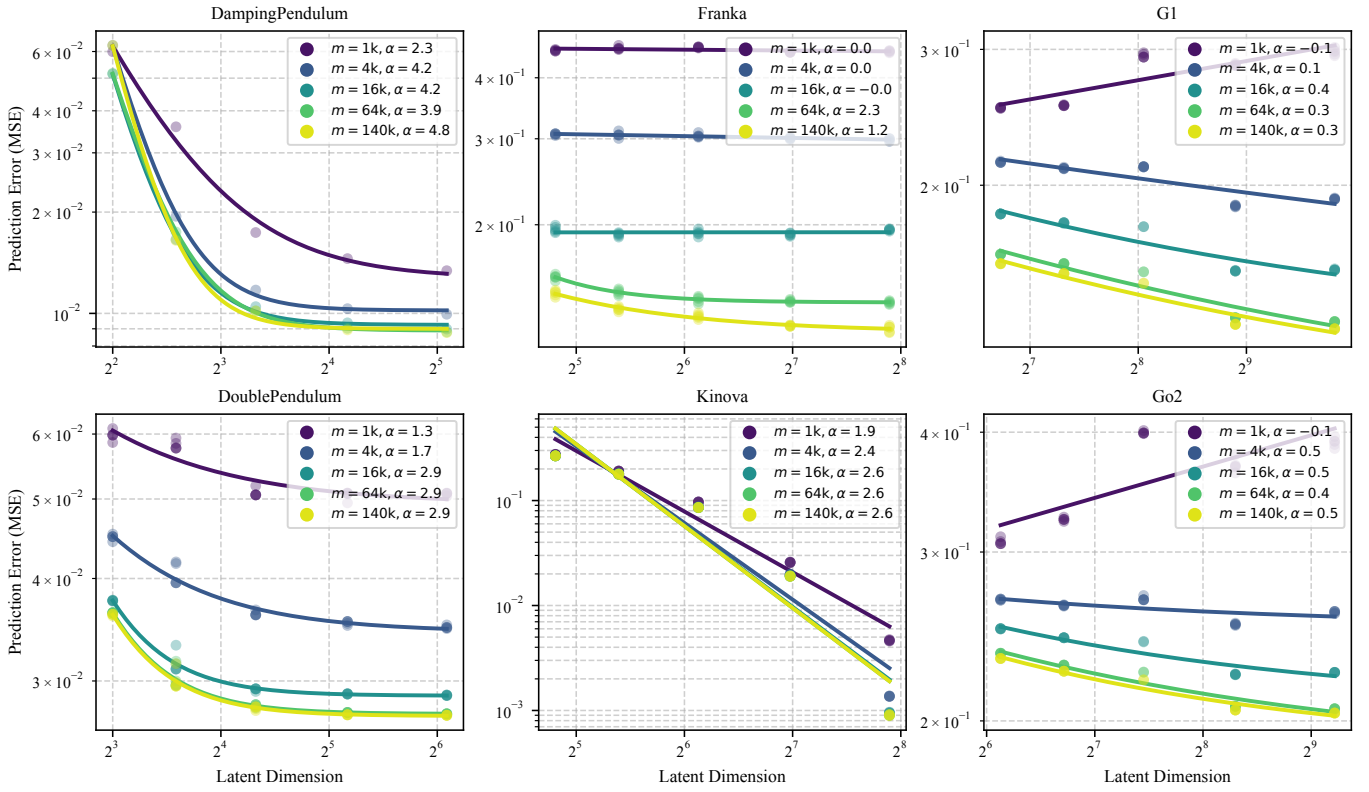


Fig. 3: Scaling of prediction error with latent dimension n . Subplots display error curves across training sample sizes (m). Increasing latent dimension generally reduces error, empirically validating projection error convergence as Koopman subspace capacity expands.

nonlinearity systems benefit most from larger latent spaces. Pendulums exhibit steep decay ($\alpha_n > 2.5$), confirming an effectively low-rank Koopman operator; energy concentrates in dominant modes, allowing compact neural embeddings to capture high-fidelity dynamics.

2) *Slow Spectral Decay (Contact-Rich Dynamics)*: Conversely, complex systems (G1, Go2) show shallower decays ($\alpha_n \in [0.34, 0.47]$), aligning with assumption 6. Locomotion’s hybrid transitions (impacts, friction) generate a “heavy tail” of high-frequency Koopman modes. Thus, projection error decays slowly, as each added dimension n captures only marginal remaining spectral energy.

3) *Over-Parameterization Regime*: For complex systems (G1, Go2), negative scaling emerges in low-data regimes (fig. 3, Right). Expanding encoder dimension at small sample sizes ($m \approx 1000$) increases prediction error. This limited data cannot constrain the expanded latent space, causing spectral pollution instead of improved fidelity. Practically, larger Koopman embeddings for contact-rich systems require commensurately larger datasets, specifically scaling as $m = \Omega(n \ln n)$ to satisfy the theoretical sample complexity in corollary 2.

3) *Unified Scaling: Balancing Data and Model Capacity*: As established previously, increasing capacity without training data causes over-parameterization, where sampling error dominates and performance degrades. To investigate optimal m and n coupling, we scaled m proportionally to model complexity, following the theoretical rate $m = \Omega(n \ln n)$ derived in corollary 2 and (30). Figure 4 illustrates prediction error for G1 and Go2 with $m = \text{coeff} \cdot n \ln n$, where coeff is

the data sufficiency coefficient. Results reveal three insights regarding sample complexity and resource allocation.

1) *Scaling Consistency*: Prediction error follows a consistent power-law decay as n increases across all coefficients. This confirms that scaling $m \propto n \ln n$ stabilizes learning, preventing the overfitting (spectral pollution) seen in the fixed- m regime.

2) *Data Sufficiency*: Increasing coeff from 1 to 40 shifts error curves downward, converging exponents toward the maximum-data baseline. For G1, coeff = 40 yields $\alpha \approx 1.58$, remarkably close to the full-data exponent ($\alpha \approx 1.50$), indicating sampling error is sufficiently suppressed to reveal intrinsic projection error.

3) *Practical Design*: We propose an empirical heuristic for high-dimensional contact-rich systems: fully leveraging a rank- n Koopman embedding requires $m \gtrsim 40 n \ln n$.

B. Effectiveness of the Proposed Auxiliary losses

To validate the regularizations from section IV-B, we evaluate the Covariance (\mathcal{L}_{cov}) and Inverse Control ($\mathcal{L}_{\text{ctrl}}$) losses on closed-loop performance. A critical finding is the decoupling of prediction accuracy and control utility: these auxiliary losses barely affect open-loop prediction error (<5% difference) but substantially improve closed-loop control.² We deployed the learned Koopman models within the MPC

²Open-loop prediction error for regularized models remained statistically similar to the baseline, indicating these losses enforce beneficial *structural properties* for control rather than improving raw *fitting* capacity.

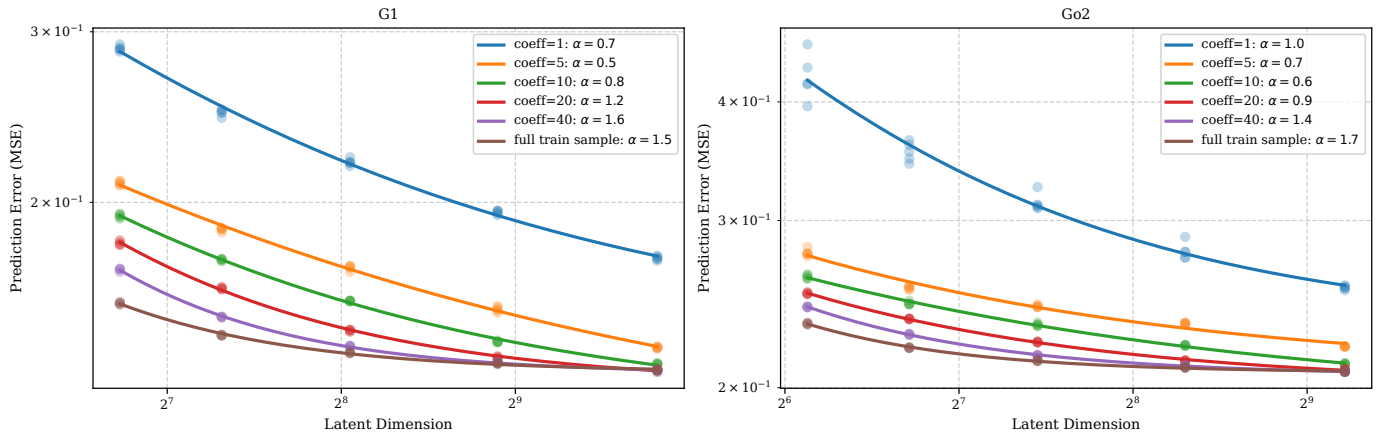


Fig. 4: Scaling of prediction error with latent dimension (n) under the coupled scaling law $m = \text{coeff} \cdot n \ln n$. As the data sufficiency coefficient increases, the error curves converge toward the asymptotic full sample baseline.

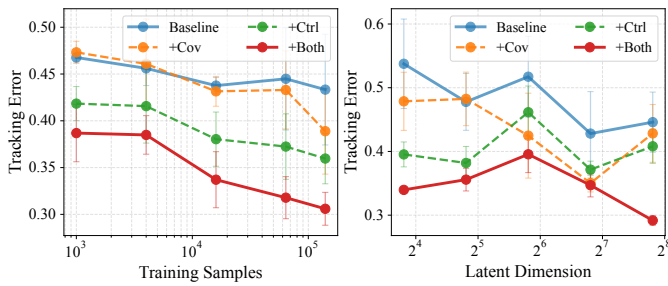


Fig. 5: Franka arm tracking error versus training samples (left) and latent dimension (right). Auxiliary losses (+Both) yield consistent performance boosts.

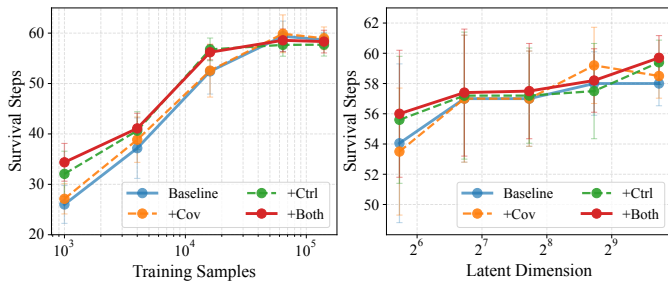


Fig. 6: G1 performance scales positively with sample size (left) and latent capacity (right). Combined auxiliary objectives (+Both) achieve the highest survival rates.

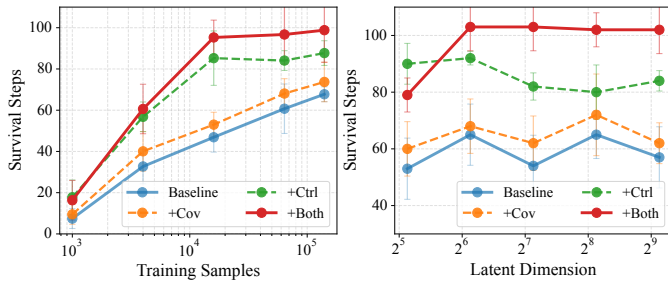


Fig. 7: Go2 control performance (survival steps). Auxiliary losses enable better scaling, especially in high-capacity regimes (right) where the baseline struggles.

framework ((56)) on the Franka arm (figure-8 tracking) and Unitree G1/Go2 robots (locomotion). Figure 5 shows that +Ctrl and +Cov individually reduce baseline tracking error, but their combination (+Both) yields the largest gain. For G1 and Go2, +Both consistently improves Mean Survival Steps across latent dimensions, whereas the baseline struggles at higher capacities (figs. 6 and 7, right).

While dynamics prediction error follows a clean power-law decay (figs. 2 and 3), control performance scaling is nuanced (figs. 5 to 7). Although larger datasets reliably improve control across all methods by reducing sampling error, increasing the latent dimension n introduces a trade-off for baseline models: higher dimensions reduce projection bias but complicate MPC optimization and inverse kinematics. Our auxiliary losses mitigate this saturation. By structurally enforcing invertibility (+Ctrl) and orthogonality (+Cov), they regularize the latent space so that expanded representational capacity does not degrade control. For instance, Go2 baseline performance plateaus early, but +Both prevents performance collapse, enabling the use of higher-dimensional representations that would otherwise be numerically intractable (fig. 7, right).

Table III summarizes these relative gains. Combining both losses substantially reduces Franka tracking error by 25.1% and increases G1 and Go2 survival steps by 9.6% and 74.8%, respectively. This massive Go2 improvement highlights the necessity of structured latent spaces for complex, underactuated quadrupedal dynamics.

TABLE III: Relative control performance improvement over baseline via Covariance (\mathcal{L}_{cov}) and Inverse Control ($\mathcal{L}_{\text{ctrl}}$) auxiliary losses.

Metrics	Environment	+ Cov loss	+ Ctrl loss	+ Both
Track Err (\downarrow)	Franka	6.18%	14.30%	25.09%
Survival Rate (\uparrow)	G1	2.09%	7.29%	9.60%
	Go2	13.6%	59.62%	74.76%

C. Ablation Studies

1) *Effectiveness of Neural Koopman Operators*: To validate the architectural choices underlying our Neural Koopman approach (specifically the use of deep learning for embedding function and the imposition of linear structure in latent

TABLE IV: Open-loop prediction error comparing classical EDMD (polynomial), unstructured Neural Dynamics (NNDM), and our Neural Koopman architecture.

Environment	EDMD (Poly)	NNDM (MLP)	Koopman (Base NN)	Koopman (+Aux)
Franka	0.441	0.268	0.122	0.121
G1	0.271	0.116	0.130	0.132
Go2	0.428	0.163	0.204	0.209

TABLE V: Closed-loop control performance comparing tracking error (Franka) and survival steps (G1, Go2). Neural Koopman combines deep learning expressivity with Linear MPC.

Metric	Env	EDMD (Poly)	NNDM (MLP)	Koopman (Base NN)	Koopman (+Aux)
Track Err(↓)	Franka	0.442	0.514	0.437	0.256
Survival(↑)	G1	34.0	27.4	58.0	59.7
	Go2	19.5	4.7	62.0	103.0

space), we compare our method against two representative baselines. 1. EDMD with Polynomial Basis (EDMD-Poly): A classical approach using fixed polynomial basis functions [44]. This represents the “structured but non-neural” baseline. 2. Unstructured Neural Dynamics (NNDM): A standard Multi-Layer Perceptron (MLP) trained to predict $x_{t+1} = f_{\theta}(x_t, u_t)$ [9]. To ensure a fair comparison of representational capacity, the NNDM is configured with the same number of parameters as our proposed Neural Koopman architecture. This represents the “neural but unstructured” baseline, which necessitates solving a non-convex nonlinear MPC problem (implemented here via random shooting with 1000 samples). In our results, NN Koopman denotes our deep Koopman architecture trained solely with the standard multi-step prediction loss ($\mathcal{L}_{\text{pred}}$). NN Koopman + Aux denotes the complete proposed method trained with the full objective, incorporating the auxiliary covariance and inverse control regularizers ($\mathcal{L}_{\text{cov}} + \mathcal{L}_{\text{inv}}$) to actively structure the latent space for control.

Table IV presents the open-loop prediction error. The standard deviation is omitted, as it is negligible (≤ 0.001) across all methods. As expected, the neural-based methods (NNDM and our Koopman NN) significantly outperform the fixed-basis EDMD, confirming that deep learning is essential for capturing the complex dynamics of high-dimensional robots. Notably, the unstructured NNDM achieves the lowest prediction error on the G1 and Go2 platforms, likely due to its unconstrained expressivity. However, superior prediction does not guarantee superior control. As shown in table V, the unstructured NNDM fails to translate its predictive accuracy into robust closed-loop performance, particularly on the high dimensional and contact rich legged robots like Go2. This failure highlights the difficulty of solving non-convex control problems in real-time. In contrast, our Neural Koopman approach, by enforcing global linearity in the latent space, allows for the use of convex Linear MPC. This guarantees a globally optimal control solution, resulting in superior survivability despite slightly higher prediction error.

2) Relationship Between Covariance Regularization and Prediction Error: Recall that our sampling error bound in proposition 1 is directly proportional to the condition number of the Gram matrix, $\kappa(G) = \frac{\lambda_{\min}}{\lambda_{\max}} \leq \frac{B^2}{\gamma}$. A well-conditioned

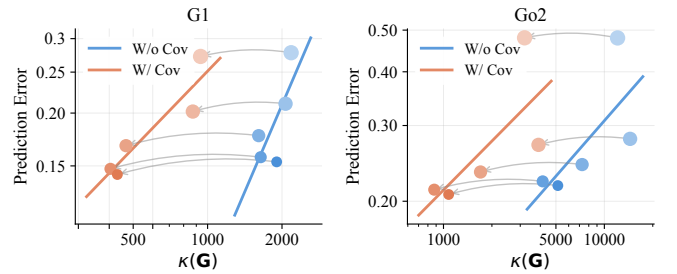


Fig. 8: Gram matrix condition number $\kappa(\mathbf{G})$ versus prediction error. Marker size and opacity denote sample size m (smaller/darker indicates larger m). Lines show fitted trends with (orange) and without (blue) covariance regularization. Grey arrows connect identical sample sizes. The proposed covariance loss significantly reduces $\kappa(\mathbf{G})$ (leftward shift) and consistently correlates with lower error.

latent space, characterized by a balanced spectrum where the minimum eigen value λ_{\min} is bounded away from zero, is a theoretical prerequisite for minimizing sampling error.

To empirically validate the theoretical link between Gram matrix condition number and model performance, we analyze the spectral properties of the empirical Gram matrix \mathbf{G} under different training regimes. Figure 8 plots the relationship between condition number $\kappa(\mathbf{G})$ and prediction error for the G1 and Go2 environments across various sample sizes (m) with largest model capacity ($n_{\text{multi}} = 16$). The results highlight two critical mechanisms. Firstly, the proposed covariance loss \mathcal{L}_{cov} (orange curve) reduces the condition number significantly compared to the baseline (blue curve). By explicitly penalizing off-diagonal terms in the Gram matrix (as defined in Eq. 53), the regularizer forces the learned observables to be nearly orthogonal. Secondly, within each method, we observe a consistent trend where increasing the sample size (indicated by smaller, darker markers) further reduces both the condition number and the prediction error. Importantly, by tracing the grey arrows connecting experiments with identical sample sizes, we observe a strict improvement: for any fixed data volume, the regularized model achieves a significantly lower condition number and reduced prediction error. These observations confirm a direct correlation between spectral stability and generalization: lower condition numbers correspond to lower prediction errors. While increasing sample size remains the dominant factor for reducing error overall, structurally enforcing orthogonality via \mathcal{L}_{cov} acts as a powerful preconditioner. It allows the model to achieve better conditioning (lower condition numbers) at any given sample size, effectively shifting the performance curve to a more favorable regime.

3) Relationship Between Inverse Control Loss and Prediction Error: While the covariance regularization \mathcal{L}_{cov} targets the stability of the state encoding via the Gram matrix, the inverse control loss \mathcal{L}_{inv} operates on the control matrix \mathbf{B} . Specifically, the explicit inverse control loss calculation relies on the pseudo-inverse $(\mathbf{B}^T \mathbf{B})^\dagger \mathbf{B}^T$, making the condition number $\kappa(\mathbf{B}^T \mathbf{B})$ a critical metric of interest.

We analyze the evolution of $\kappa(\mathbf{B}^T \mathbf{B})$ under different training regimes ($n_{\text{multi}} = 16$, varying sample sizes) for G1 and Go2 environments. Figure 9 reveals a fundamentally different behavior compared to the Gram matrix analysis in the previous section. Unlike the Gram matrix, we observe that the condition

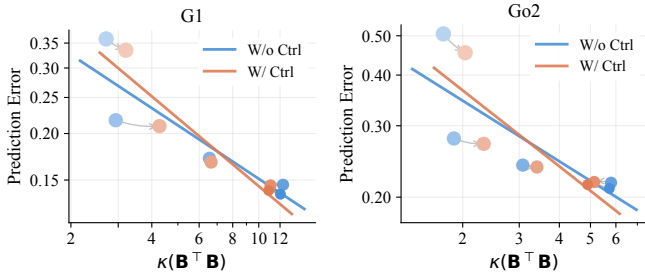


Fig. 9: Control matrix condition number $\kappa(\mathbf{B}^\top \mathbf{B})$ versus prediction error. Marker size/opacity denote sample size m (smaller/darker indicates larger m), and grey arrows connect identical sample sizes. Lines show fitted trends with (orange) and without (blue) inverse control regularization. Unlike the Gram matrix, $\kappa(\mathbf{B}^\top \mathbf{B})$ correlates negatively with error; better models naturally evolve higher condition numbers.

number of the control matrix, $\kappa(\mathbf{B}^\top \mathbf{B})$, increases as the model converges to lower prediction errors. This trend is physically consistent with the dynamics of underactuated systems such as the G1 and Go2. In the initial training phases or low-data regimes, the matrix \mathbf{B} is often initialized near-isotropically (low κ). As the model captures the true dynamics with more sample size, it must reflect the highly anisotropic nature of the robot’s physical actuation—where certain latent directions possess high control authority (large eigenvalues) while others are underactuated (small eigenvalues). In addition, while the inverse control loss (Green curve) does not shift the global distribution as drastically as the covariance loss, its impact is highly data size dependent. When sample size is small ($m \approx 10^3$), the explicit regularization of \mathcal{L}_{inv} provides a critical structural prior. We observe that the regularized models (Orange) achieve lower prediction errors and higher condition numbers compared to the baseline (Blue). As the sample size increases ($m \rightarrow 10^5$), the two curves converge. In this regime, the abundance of interaction data allows the baseline model to naturally recover the correct anisotropic structure of \mathbf{B} via the prediction loss.

Additionally, to empirically validate the proposed scaling laws against a controlled ground truth, we present a case study analyzing system nonlinearity and scaling behavior in Supplementary Section 2.

VII. CONCLUSION

In this work, we investigated the fundamental scaling laws of Neural Koopman Operators. By theoretically decomposing the estimation error, we showed that sampling error decays with training sample size (m), while projection error decays with latent embedding dimension (n). Consequently, optimal scaling requires expanding the latent dimension alongside the dataset size. Guided by this analysis, we introduced Covariance and Inverse Dynamics regularization losses to structurally enforce orthogonality and invertibility within the learned subspace. Our empirical evaluation, spanning simple pendulums to high-dimensional legged robots (G1 and Go2), validates these scaling relationships and demonstrates that our regularizers maintain robust closed-loop control even in data-limited, contact-rich regimes.

Future work will focus on three directions: 1. Relaxing Assumptions: Extending our error bounds beyond standard i.i.d. and spectral decay assumptions to rigorously account for the non-stationary trajectories and hybrid contact dynamics inherent in real-world locomotion. 2. Dynamics Foundation Models: Leveraging our capacity scaling insights to train on massive, multi-embodiment datasets, aiming to develop a general-purpose model capable of transferring universal physical invariants across different robot morphologies. 3. Sim-to-Real Deployment: Validating our architecture on physical G1 and Go2 hardware, integrating online adaptation mechanisms to mitigate real-world sensing noise and further lower the irreducible error floor.

ACKNOWLEDGMENT

The authors thank Hongyi Chen for insightful discussions on Koopman operator theory and Zhongqi Wei for collecting the Kinova dataset. This work was supported by the National Science Foundation (NSF) under Grant 2144489.

- [1] H. K. Khalil and J. W. Grizzle, *Nonlinear systems*. Prentice hall Upper Saddle River, NJ, 2002, vol. 3.
- [2] T. He, Z. Luo, W. Xiao, C. Zhang, K. Kitani, C. Liu, and G. Shi, “Learning human-to-humanoid real-time whole-body teleoperation,” in *2024 IEEE/RSJ International Conference on Intelligent Robots and Systems (IROS)*. IEEE, 2024, pp. 8944–8951.
- [3] T. Haarnoja, A. Zhou, P. Abbeel, and S. Levine, “Soft actor-critic: Off-policy maximum entropy deep reinforcement learning with a stochastic actor,” in *International conference on machine learning*. PMLR, 2018, pp. 1861–1870.
- [4] Z. Fu, Q. Zhao, Q. Wu, G. Wetzstein, and C. Finn, “Humanplus: Humanoid shadowing and imitation from humans,” in *Conference on Robot Learning*. PMLR, 2025, pp. 2828–2844.
- [5] A. S. Polydoros and L. Nalpantidis, “Survey of model-based reinforcement learning: Applications on robotics,” *Journal of Intelligent & Robotic Systems*, vol. 86, no. 2, pp. 153–173, 2017.
- [6] D. Q. Mayne, J. B. Rawlings, C. V. Rao, and P. O. Scokaert, “Constrained model predictive control: Stability and optimality,” *Automatica*, vol. 36, no. 6, pp. 789–814, 2000.
- [7] S. Katayama, M. Murooka, and Y. Tazaki, “Model predictive control of legged and humanoid robots: models and algorithms,” *Advanced Robotics*, vol. 37, no. 5, pp. 298–315, 2023.
- [8] H. Kazemi, V. J. Majd, and M. M. Moghaddam, “Modeling and robust backstepping control of an underactuated quadruped robot in bounding motion,” *Robotica*, vol. 31, no. 3, p. 423–439, 2013.
- [9] A. Nagabandi, G. Kahn, R. S. Fearing, and S. Levine, “Neural network dynamics for model-based deep reinforcement learning with model-free fine-tuning,” in *2018 IEEE international conference on robotics and automation (ICRA)*. IEEE, 2018, pp. 7559–7566.
- [10] A. Abuduweili, S. Li, and C. Liu, “Adaptable human intention and trajectory prediction for human-robot collaboration,” in *AAAI Fall Symposium on Artificial Intelligence and Human-Robot Interaction*, 2019.
- [11] A. Abuduweili and C. Liu, “Robust nonlinear adaptation algorithms for multitask prediction networks,” *International Journal of Adaptive Control and Signal Processing*, vol. 35, no. 3, pp. 314–341, 2021.
- [12] B. O. Koopman, “Hamiltonian systems and transformation in hilbert space,” *Proceedings of the National Academy of Sciences*, vol. 17, no. 5, pp. 315–318, 1931.
- [13] I. Mezić, “Spectral properties of dynamical systems, model reduction and decompositions,” *Nonlinear Dynamics*, vol. 41, pp. 309–325, 2005.
- [14] C. W. Rowley, I. Mezić, S. Bagheri, P. Schlatter, and D. S. Henningson, “Spectral analysis of nonlinear flows,” *Journal of fluid mechanics*, vol. 641, pp. 115–127, 2009.
- [15] M. O. Williams, I. G. Kevrekidis, and C. W. Rowley, “A data-driven approximation of the koopman operator: Extending dynamic mode decomposition,” *Journal of Nonlinear Science*, vol. 25, no. 6, pp. 1307–1346, 2015.

- [16] C. A. Johnson, S. Balakrishnan, and E. Yeung, "Heterogeneous mixtures of dictionary functions to approximate subspace invariance in koopman operators: Why deep koopman operators works," *Journal of Nonlinear Science*, vol. 35, no. 4, p. 68, 2025.
- [17] B. Lusch, J. N. Kutz, and S. L. Brunton, "Deep learning for universal linear embeddings of nonlinear dynamics," *Nature communications*, vol. 9, no. 1, p. 4950, 2018.
- [18] E. Yeung, S. Kundu, and N. Hodas, "Learning deep neural network representations for koopman operators of nonlinear dynamical systems," in *2019 American Control Conference (ACC)*. IEEE, 2019, pp. 4832–4839.
- [19] J. Kim, Y. Han, H. Ravichandar, and S. Ha, "Learning koopman dynamics for safe legged locomotion with reinforcement learning-based controller," *arXiv preprint arXiv:2409.14736*, 2024.
- [20] M. Korda and I. Mezić, "Linear predictors for nonlinear dynamical systems: Koopman operator meets model predictive control," *Automatica*, vol. 93, pp. 149–160, 2018.
- [21] H. Chen, A. Abuduweili, A. Agrawal, Y. Han, H. Ravichandar, C. Liu, and J. Ichnowski, "Korol: Learning visualizable object feature with koopman operator rollout for manipulation," in *Conference on Robot Learning*. PMLR, 2025, pp. 4509–4524.
- [22] F. Nüske, S. Peitz, F. Philipp, M. Schaller, and K. Worthmann, "Finite-data error bounds for koopman-based prediction and control," *Journal of Nonlinear Science*, vol. 33, no. 1, p. 14, 2023.
- [23] M. J. Colbrook and A. Townsend, "Rigorous data-driven computation of spectral properties of koopman operators for dynamical systems," *Communications on Pure and Applied Mathematics*, vol. 77, no. 1, pp. 221–283, 2024.
- [24] G. Mamakoukas, M. L. Castano, X. Tan, and T. D. Murphey, "Derivative-based koopman operators for real-time control of robotic systems," *IEEE Transactions on Robotics*, vol. 37, no. 6, pp. 2173–2192, 2021.
- [25] F. Li, A. Abuduweili, Y. Sun, R. Chen, W. Zhao, and C. Liu, "Continual learning and lifting of koopman dynamics for linear control of legged robots," in *7th Annual Learning for Dynamics & Control Conference*. PMLR, 2025, pp. 136–148.
- [26] C.-M. Yang and P. A. Bhounsule, "Koopman operator based linear model predictive control for quadruped trotting," in *2025 IEEE International Conference on Robotics and Automation (ICRA)*. IEEE, 2025, pp. 12 359–12 364.
- [27] J. Kaplan, S. McCandlish, T. Henighan, T. B. Brown, B. Chess, R. Child, S. Gray, A. Radford, J. Wu, and D. Amodei, "Scaling laws for neural language models," *arXiv preprint arXiv:2001.08361*, 2020.
- [28] J. Hoffmann, S. Borgeaud, A. Mensch, E. Buchatskaya, T. Cai, E. Rutherford, D. de Las Casas, L. A. Hendricks, J. Welbl, A. Clark *et al.*, "Training compute-optimal large language models," in *Proceedings of the 36th International Conference on Neural Information Processing Systems*, 2022, pp. 30 016–30 030.
- [29] B. Zitkovich, T. Yu, S. Xu, P. Xu, T. Xiao, F. Xia, J. Wu, P. Wohlhart, S. Welker, A. Wahid *et al.*, "Rt-2: Vision-language-action models transfer web knowledge to robotic control," in *Conference on Robot Learning*. PMLR, 2023, pp. 2165–2183.
- [30] A. Kumar, R. Agarwal, X. Geng, G. Tucker, and S. Levine, "Offline q-learning on diverse multi-task data both scales and generalizes," in *The Eleventh International Conference on Learning Representations*, 2023.
- [31] F. Lin, Y. Hu, P. Sheng, C. Wen, J. You, and Y. Gao, "Data scaling laws in imitation learning for robotic manipulation," in *The Thirteenth International Conference on Learning Representations*, 2025.
- [32] M. O. Williams, I. G. Kevrekidis, and C. W. Rowley, "A data-driven approximation of the koopman operator: Extending dynamic mode decomposition," *Journal of Nonlinear Science*, p. 1307–1346, Dec 2015.
- [33] M. Korda and I. Mezić, "On convergence of extended dynamic mode decomposition to the koopman operator," *Journal of Nonlinear Science*, vol. 28, pp. 687–710, 2018.
- [34] A. Lasota and M. C. Mackey, *Chaos, fractals, and noise: stochastic aspects of dynamics*. Springer Science & Business Media, 2013, vol. 97.
- [35] J. A. Tropp *et al.*, "An introduction to matrix concentration inequalities," *Foundations and Trends® in Machine Learning*, vol. 8, no. 1-2, pp. 1–230, 2015.
- [36] J. A. Tropp, "User-friendly tail bounds for sums of random matrices," *Foundations of computational mathematics*, vol. 12, pp. 389–434, 2012.
- [37] K. Knopp, *Infinite sequences and series*. Courier Corporation, 2012.
- [38] K. Hornik, M. Stinchcombe, and H. White, "Multilayer feedforward networks are universal approximators," *Neural networks*, vol. 2, no. 5, pp. 359–366, 1989.
- [39] G. Cybenko, "Approximation by superpositions of a sigmoidal function," *Mathematics of control, signals and systems*, vol. 2, no. 4, pp. 303–314, 1989.
- [40] L. N. Trefethen, *Approximation theory and approximation practice, extended edition*. SIAM, 2019.
- [41] A. Mauroy and I. Mezić, "Global stability analysis using the eigenfunctions of the koopman operator," *IEEE Transactions on Automatic Control*, vol. 61, no. 11, pp. 3356–3369, 2016.
- [42] N. Rahaman, A. Baratin, D. Arpit, F. Draxler, M. Lin, F. Hamprecht, Y. Bengio, and A. Courville, "On the spectral bias of neural networks," in *International conference on machine learning*. PMLR, 2019, pp. 5301–5310.
- [43] H. Shi and M. Q.-H. Meng, "Deep koopman operator with control for nonlinear systems," *IEEE Robotics and Automation Letters*, vol. 7, no. 3, pp. 7700–7707, 2022.
- [44] Y. Han, M. Xie, Y. Zhao, and H. Ravichandar, "On the utility of koopman operator theory in learning dexterous manipulation skills," in *Conference on Robot Learning*. PMLR, 2023, pp. 106–126.

APPENDIX

A. Experimental Setup

We validate our approach on seven dynamical systems exhibiting a wide range of complexities, from simple nonlinearities to high-dimensional robotic locomotion. Table VI summarizes the dimensions for each environment used in the main experiment.

TABLE VI: Summary of environments and original dimensions. Note that the Unitree G1 and Go2 models are trained on trimmed state–action spaces.

Environment	State Dim.	Action Dim.
Polynomial	3	0
Damping Pendulum	2	1
Double Pendulum	4	2
Franka Panda	14	7
Kinova Gen3	14	7
Unitree Go2	35	12
Unitree G1	53	23

a) *Polynomial System*: To empirically validate the proposed scaling laws against a controlled ground-truth setting, we consider a 3D discrete-time polynomial system with tunable nonlinear coupling:

$$\begin{aligned} x_{1,t+1} &= 0.85 x_{1,t}, \\ x_{2,t+1} &= 0.90 x_{2,t}, \\ x_{3,t+1} &= 0.90 x_{3,t} + \sum_{p=1}^{n_{\text{poly}}-2} b_p x_{1,t}^p, \end{aligned} \quad (58)$$

where n_{poly} controls the maximum degree of the polynomial interaction term, and b_p is a scaling coefficient (e.g., $b_p = 0.9$). Increasing n_{poly} directly increases the effective nonlinear complexity of the system while preserving stability. Following Strategy I (Section IV.C), trajectories are generated from initial states sampled uniformly from the hypercube $[-1, 1]^3$.

b) *Damping & Double Pendulums*: To evaluate performance on physically meaningful nonlinear systems, we consider two classical nonlinear control benchmarks: a damped pendulum and a double pendulum. For the Damped Pendulum, the state $x \in \mathbb{R}^2$ consists of angle and angular velocity, while for the Double Pendulum, $x \in \mathbb{R}^4$ comprises angles and velocities for both joints. In both cases, the control $u \in \mathbb{R}$ represents the torque applied to the primary joint. These continuous-time dynamics are simulated via numerical integration (using `scipy.integrate.odeint`), with time discretization $\Delta t = 0.02\text{s}$ (damped pendulum) and $\Delta t = 0.01\text{s}$ (double pendulum). Training trajectories are generated using Strategy I by sampling initial states uniformly within predefined state bounds and applying randomized control inputs at each time step.

c) *Franka Panda (Simulation)*: We evaluate our approach on a simulated 7-DoF Franka Emika Panda manipulator in PyBullet. The system state $x \in \mathbb{R}^{14}$ comprises 7 joint positions, and 7 joint velocities. The control input $u \in \mathbb{R}^7$ corresponds to commanded joint velocities. Note that, the commanded joint velocities do not directly equal the measured joint velocities due to internal low-level tracking dynamics, introducing a realistic actuation discrepancy. Since the simulator imposes

no safety constraints, data is generated following Strategy II (randomized actuation). The robot is initialized near a nominal home configuration with small random joint perturbations, and trajectories are collected by applying randomly sampled joint velocity commands.

d) *Kinova Gen3 (Real World)*: To evaluate performance on physical hardware, we deploy our method on Kinova Gen3, a lightweight 7-DoF collaborative manipulator. The state $x \in \mathbb{R}^{14}$ includes joint positions and velocities, while the control input $u \in \mathbb{R}^7$ consists of commanded joint velocities. Unlike the simulation setting, real-world data collection requires strict safety guarantees. We therefore adopt Strategy III (constrained exploration). Using the Drake robotics toolbox, we formulate a two-stage kinematic trajectory optimization procedure. First, a feasible trajectory is computed between randomly sampled configurations. Second, the trajectory is refined to enforce collision avoidance and joint-limit constraints. This structured data collection process ensures sufficient state-space coverage while preventing unsafe motions and hardware damage.

e) *Unitree Go2 & G1 (Simulation)*: We further evaluate scalability on high-dimensional, underactuated locomotion systems: the Unitree Go2 quadruped and the Unitree G1 humanoid, simulated in Isaac Sim. These platforms exhibit complex hybrid dynamics and underactuation, providing a challenging testbed for learning-based Koopman models. For both systems, the state x includes base orientation (quaternion), base linear and angular velocities, and joint positions and velocities. The control input u consists of desired joint positions executed through embedded PD controllers. Data is generated using the expert-guided exploration strategy (Strategy III). We first collect a baseline dataset using a pretrained RL-trained expert policy. We then perform iterative data aggregation: a Koopman-based MPC controller tracks expert-generated trajectories, and the resulting on-policy rollouts are incorporated into the training set. By combining expert demonstrations with on-policy recovery data, the learned model is exposed to the state distributions and stabilization behaviors encountered during closed-loop deployment.

B. Case Study: System Nonlinearity and Scaling Law

To empirically validate the proposed scaling laws against a controlled ground-truth setting, we consider a 3D discrete-time polynomial system with tunable nonlinear coupling:

$$\begin{aligned} x_{1,t+1} &= 0.85 x_{1,t}, \\ x_{2,t+1} &= 0.90 x_{2,t}, \\ x_{3,t+1} &= 0.90 x_{3,t} + \sum_{p=1}^{n_{\text{poly}}-2} b_p x_{1,t}^p, \end{aligned} \quad (59)$$

where n_{poly} controls the maximum degree of the polynomial interaction term, and b_p is a scaling coefficient (e.g., $b_p = 0.9$). Increasing n_{poly} directly increases the effective nonlinear complexity of the system while preserving stability. Following Strategy I (Section IV.C), trajectories are generated from initial states sampled uniformly from the hypercube $[-1, 1]^3$.

We use the polynomial system in (59) as a controlled test case to understand how physical nonlinearity affects scaling

law of neural Koopman operators. We test five different levels of nonlinearity, setting the polynomial degree $n_{\text{poly}} \in \{3, 5, 10, 20, 50\}$. For each level, we fit the prediction error to the power-law $\epsilon(D) = AD^{-\alpha} + C$. To ensure accurate fits, we isolate the variables as follows. For Sample Scaling (α_m), We vary sample size m while keeping the model capacity fixed at its maximum ($n_{\text{multi}} = 16$). For latent dimension scaling (α_n), We vary latent dimension n while keeping the dataset size fixed at its maximum ($m = 140\text{k}$).

TABLE VII: Impact of Nonlinearity on Scaling. Higher n_{poly} leads to slower exponent decay term (lower α) and higher error floors (C). R^2 indicates fit reliability.

n_{poly}	Sample Size (α_m, C_m, R^2)	Latent Dim (α_n, C_n, R^2)
3	(2.64, 1.75×10^{-8} , 1.00)	(0.28, 1.18×10^{-21} , 0.25)
5	(2.57, 8.79×10^{-8} , 1.00)	(0.20, 2.72×10^{-21} , 0.51)
10	(2.52, 4.74×10^{-7} , 1.00)	(0.14, 4.51×10^{-20} , 0.74)
20	(1.91, 2.98×10^{-6} , 1.00)	(0.08, 4.54×10^{-20} , 0.57)
50	(1.64, 2.63×10^{-5} , 0.99)	(0.02, 4.17×10^{-19} , 0.53)

Table VII summarizes the results. The trends tell a clear story about how complexity related to scaling law. As the nonlinearity n_{poly} increases from 3 to 50, the scaling exponent α_m drops ($2.64 \rightarrow 1.64$). This means highly nonlinear systems are “data-hungry”, that is they require exponentially more samples to achieve the same reduction in error. Simultaneously, the error floor C_m rises by orders of magnitude. This confirms that for complex systems, the error quickly becomes *bias-limited*: even with infinite data, a finite model struggles to capture the whole dynamics of a high-degree polynomial. The error floor C_m includes the projection error. The latent dimension scaling follows a similar pattern but with much smaller exponents. As nonlinearity increases, α_n decays. This happens because high-degree polynomials have a “heavy-tailed” spectrum (as discussed in assumption 6); the system’s energy is spread across infinitely many modes. Consequently, adding more latent dimensions yields diminishing returns because each new dimension captures only a tiny fraction of the remaining dynamics.

We then evaluate if our proposed covariance loss (\mathcal{L}_{cov}) is effective in the polynomial system. We compared performance on the largest setting ($m = 140\text{k}$, $n_{\text{multi}} = 16$). As shown in Table VIII, the covariance loss consistently reduces error. The improvement is largest for the most nonlinear cases. As related to Assumption 4, this suggests that \mathcal{L}_{cov} forces the network to learn independent feature vectors, allowing it to acquire more useful information within the limited latent space, which is a critical advantage when the dynamics are complex.

TABLE VIII: Impact of covariance regularization loss (\mathcal{L}_{cov}) on prediction error. Evaluated across varying polynomial degrees (n_{poly}) on largest model capacity ($n_{\text{multi}} = 16$) and dataset size ($m = 140\text{k}$).

Degree (n_{poly})	Baseline	+ Cov loss	Error Reduction
3	9.51×10^{-6}	8.89×10^{-6}	6.5%
5	2.12×10^{-5}	2.04×10^{-5}	4%
10	6.22×10^{-4}	5.47×10^{-4}	12.1%
20	1.34×10^{-2}	1.17×10^{-2}	12.7%
50	1.98×10^{-1}	1.62×10^{-1}	18.1%

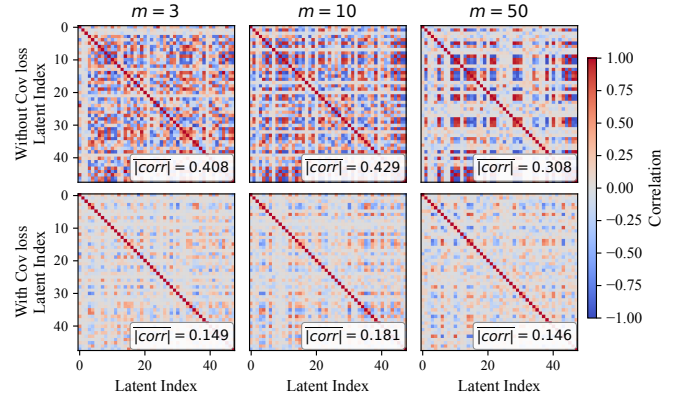


Fig. 10: Impact of Covariance Regularization on Latent Feature Correlation. Heatmaps display the correlation matrices of the learned embeddings $\phi(x)$ for varying polynomial degrees $n_{\text{poly}} \in \{3, 10, 50\}$. Top Row (Baseline): Without regularization, features exhibit high cross-correlation (dense off-diagonal blocks). Bottom Row (w/ \mathcal{L}_{cov}): With regularization, the matrices become significantly sparser, demonstrating effective feature decorrelation. The mean off-diagonal correlation $|\overline{\text{corr}}|$ is reported for each case.

To visualize the mechanism behind the performance gains reported in Table VIII, we analyze the structural independence of the learned embedding functions. We compute the correlation matrix between the latent feature vectors $\{\phi_i\}_{i=1}^n$ for the high-capacity regime ($n = 48, m = 140\text{k}$). Figure 10 compares the correlation structures for systems with increasing nonlinearity ($n_{\text{poly}} \in \{3, 10, 50\}$). As shown in top row, without covariance regularization, the baseline models exhibit significant spectral redundancy. The heatmaps show dense off-diagonal blocks with high correlation coefficients ($|\overline{\text{corr}}| > 0.30$). This indicates that many latent dimensions are effectively encoding the same dominant modes. As shown in the bottom row, applying the covariance loss significantly alters the feature structure. The heatmaps become sparse and diagonally dominant, with the mean off-diagonal correlation dropping below 0.19. This confirms that \mathcal{L}_{cov} successfully enforces orthogonality in the function space. This maximizes the effective rank of the Koopman operator and ensures that each dimension contributes unique information to the prediction. This empirical decorrelation directly supports the validity of Assumption 4, thereby stabilizing the scaling laws and enabling continuous performance improvements as model capacity increases.